Partition of mixed modes in double cantilever beams with non-rigid elastic interfaces

Partition of mixed modes in layered isotropic double cantilever beams with non-rigid cohesive interfaces

S. Wang*, C. M. Harvey and L. Guan

Department of Aeronautical and Automotive Engineering, Loughborough University, Loughborough, Leicestershire LE11 3TU, United Kingdom

Abstract

The authors' existing mixed-mode partition theories for rigid interfaces are extended to non-rigid cohesive interfaces for layered isotropic double cantilever beams. Within the context of Euler beam theory, it is shown that the two sets of orthogonal pure modes coincide at the first set of pure modes due to the absence of any crack tip stress singularity for a non-rigid interface. The total energy release rate in a mixed mode is then partitioned using this first set of pure modes without considering any 'stealthy interaction'. Within the context of Timoshenko beam theory, it is shown that the mode II component of energy release rate is the same as that in Euler beam theory while the mode I component is different due to the through-thickness shear effect. Within the context of 2D elasticity, a mixed-mode partition theory is developed using the two sets of orthogonal pure modes from Euler beam theory with rigid interfaces and a powerful orthogonal pure mode methodology. Numerical simulations are conducted to verify the theories.

Keywords: Cohesive interfaces, Energy release rate, Mixed-mode partitions, Non-rigid interfaces, Orthogonal pure modes

1. Introduction

Delamination is of major concern in the application of laminated composite materials and layered materials more generally. Although it often occurs together with other damage modes such as fiber breakage, matrix cracking and intralaminar cracking, pure delamination is an important research topic that provides insightful understanding of laminar interfacial mechanics. One-dimensional delamination is the most common pure delamination scenario, where delaminations propagate in one dimension only and usually consists of only opening mode I and shearing mode II. Some practical examples of one-dimensional delamination are given in the next paragraph. In the following, delamination is simply referred to as 'fracture' in order to keep consistency with the description of fracture mechanics.

Study of one-dimensional fracture has great importance: It is often used in experimental tests, such as the double cantilever beam (DCB), end-loaded split (ELS) and end-notched flexure (ENF) tests, to obtain the critical energy release rate (ERR)—or 'fracture toughness'—of a material in either pure mode I or mode II fracture. In the case of a mixed mode, it is often used to investigate fracture propagation criteria. Moreover, many practical fractures in materials can be

* Corresponding Author
Email addresses: s.wang@lboro.ac.uk (S. Wang), c.m.harvey@lboro.ac.uk (C. M. Harvey), l.guan2@lboro.ac.uk (L. Guan)

Nomenclature

a	crack length in a DCB
A_1, A_2	cross-sectional areas of upper and lower beams
b	width of a DCB
E	Young's modulus
F_n	resultant normal force in crack influence zone
G_{xz}	through-thickness shear modulus
G, G_I, G_{II}	total, mode I and mode II energy release rates
G^{MN}, G_I^{MN}, G_{II}^{MN}	energy release rates due to crack tip bending moments and axial forces
G^{NR}, G_I^{NR}, G_{II}^{NR}	energy release rates for non-rigid interfaces
G^P, G_I^P, G_{II}^P	energy release rates due to crack tip shear forces
G^R, G_I^R, G_{II}^R	energy release rates for rigid interfaces
G_θ, $G_{\beta'}$, G_β	θ mode I, β' and β mode II energy release rates
h_1, h_2, h	thicknesses of upper, lower and intact beams or plates
I_1, I_2	second moments of area of upper and lower beams
k^2	through-thickness shear correction factor
k_{er}	interface stiffness to Young's modulus ratio
k_s	interface spring stiffness
k_σ	interface penalty stiffness for opening stress
k_τ	interface penalty stiffness for shear stress
L	length of a DCB
M_n	resultant moment in crack influence zone
M_1, M_2	DCB tip bending moments on upper and lower beams
M_{1B}, M_{2B}	crack tip bending moments on upper and lower beams
N_1, N_2	DCB tip axial forces on upper and lower beams
N_{1B}, N_{2B}	crack tip axial forces on upper and lower beams
N_{1Be}	crack tip effective axial force on upper beam
P_1, P_2	DCB tip shear forces on upper and lower beams
P_{1B}, P_{2B}	crack tip shear forces on upper and lower beams
$\overline{u}$, $\overline{w}$	relative shearing and opening displacements at interface
α_θ, α_β	mixed-mode partition coefficients for θ mode I and β mode II
β, β'	β and β' pure modes II
γ	thickness ratio
θ, θ'	θ and θ' pure modes I
σ_n, τ_s	interface normal and shear stresses
Δa	crack influence length in a DCB
ΔG	pure mode interaction

Abbreviations	
COH2D4	four-node quadrilateral cohesive element
DCB	double cantilever beam
ELS	end-loaded split
ENF	end-notched flexure
ERR	energy release rate
FEM	finite element method
QUAD4	four-node plane-stress quadrilateral with linear displacement field

approximated as one-dimensional fracture. The most common ones are through-width fracture in straight or curved laminated composite beams, circular ring-type fracture in laminated composite plates and shells which may arise for example during drilling, separation of two material layers in a biological cell which may arise for example during needle puncture, separation of stiffeners and skins in stiffened-plate or stiffened-shell panels, etc.

One-dimensional fracture has attracted the attention of many researchers. The primary goals have been to develop analytical theories to find pure fracture modes and then to partition a mixed mode into pure modes. Most of the previous analytical studies have focused on fractures with rigid interfaces. That is, no relative separation occurs at the interface before fracture happens, which results in a stress singularity at the crack tip. Some important pioneering work was given by Williams [1] for DCBs made of isotropic materials and based on Euler beam theory. A pair of pure mode I and II modes were correctly given in the absence of axial loads. However, the partition of a mixed mode was limited to symmetric DCBs. Another piece of pioneering work was given by Schapery and Davidson [2], which was also for DCBs based on Euler beam theory. Their work [2] was a combined numerical and analytical method. It does not give the Williams [1] pair of pure modes. It also reported that Euler beam theory does not provide quite enough information to obtain a decomposition of ERR into opening and shearing mode components. Suo and Hutchinson [3] and Hutchinson and Suo [4] reported their work on isotropic DCBs, which used a combined approach with Euler beam theory and 2D elasticity, with stress intensity factors. Their work [3,4] gave a combined numerical and analytical theory. Hutchinson and Suo [4] commented that the work in Ref. [1] contained conceptual errors. To respond to this comment some experimental work was reported in Ref. [5] showing that the mixed mode partition rule in Ref. [1] agrees better with the test results than the rule in Refs. [3,4] does. Some other earlier research articles are given in Refs. [6,7]. Several recent research articles on the topic are quoted here among many others. Wang and Qiao [8] developed a similar approach to that in Refs. [3,4] to study interface cracking between two shear-deformable elastic layers of a DCB. Refs. [9,10] reported an empirical mixed-mode partition theory for DCBs based on numerical simulations. All the above studies assumed rigid fracture interfaces. Ouyang and Li [11] developed an analytical method to study the non-linear interface shear fracture of ENF specimens of bilayer materials. Their theory [11] agrees well with experimental results. Very recently, the mixed-mode fracture of single leg bending (SLB) beams with two sub-layers of equal thickness was considered in Ref. [12]. In this work [12], interfacial constitutive laws were studied with various adhesive thicknesses using experimental tests and some interesting results were presented. The authors of Ref. [12] also reported a study on opening mode fracture between bonded dissimilar materials [13]. Nguyen and Levy [14] reported an exact theory of interfacial debonding in layered elastic composites using Fourier series solutions. The theory in Ref. [14] results in a system of non-linear algebraic equations, and numerical solution procedures are required. A mixed-mode partition theory was given in Ref. [15] based on an enhanced beam model and interface springs. Refs. [16,17] reported finite fracture mechanics on elastic interfaces [16] which are represented by linear springs and adhesive joints [17].

On the subject of numerical simulation, the interface spring model [18,19] has proven to be an accurate approach to partition mixed-mode fractures on rigid interfaces; the cohesive model [20,21] has proven to be an accurate approach for cohesive interfaces. It is worth noting that Valvo [22] recently derived an improved virtual crack closure technique for ERR calculations. There are also a large number of experimental studies on the topic. Some representative work is given in Refs. [23-25].

Recently, the authors have developed completely analytical theories for one-dimensional fractures in laminated composite beams, plates and shells with rigid interfaces using a completely new approach. The theories were first developed for DCBs [26,27]. Further publications are given in Refs. [28-34]. The developed theory has been fully validated by using finite element method (FEM) simulations. Interested readers are referred to Refs. [29-34] for details about FEM validation and comments on Refs. [1-4].

In this paper the theories are extended to layered isotropic DCBs with non-rigid linear elastic interfaces and non-rigid non-linear elastic interfaces within the contexts of both the Euler and Timoshenko beam theories. If it is assumed that the crack separates monotonically, that is, no unloading or crack closure, the theories are also applicable to non-rigid plastic interfaces with the dissipated plastic energy taken as part of the released energy. Within the context of 2D elasticity theory, the partition theory for rigid interfaces is extended to consider interface constitutive laws with both a linear elastic part and either a linear or non-linear softening part. In the following development, the term 'non-rigid cohesive interface' is used to refer generally to both non-rigid elastic interfaces and non-rigid plastic interfaces.

2. Theories

2.1. Brief summary of mixed-mode partitioning with rigid interfaces [31,33]

Fig. 1a shows a DCB with its geometry and tip loadings. The crack influence zone extends to a point A, a Δa-distance ahead of the crack tip B. Fig. 1b only shows the sign convention of the interface normal stress σ_n and shear stress τ_s instead of any representative distribution within the crack influence zone. Beyond point A, the normal stress σ_n becomes zero and the shear stress τ_s is the same at that in a normal beam. Note that the terminology 'crack influence zone' is used instead of the conventional 'cohesive zone'. One reason for this is to keep consistency with Refs. [31, 33]. Without considering the contribution from the crack tip shear forces P_{1B} and P_{2B}, the ERR G^R can be written as

$$\begin{aligned} G^R &= \frac{1}{2Eb}\left[\frac{M_{1B}^2}{I_1}+\frac{M_{2B}^2}{I_2}-\frac{1}{I}\left(M_{1B}+M_{2B}-\frac{h_2 N_{1Be}}{2}\right)^2+\left(\frac{1}{A_1}-\frac{1}{A}\right)N_{1Be}^2\right] \\ &= \begin{Bmatrix} M_{1B} & M_{2B} & N_{1Be} \end{Bmatrix}[C]\begin{Bmatrix} M_{1B} & M_{2B} & N_{1Be} \end{Bmatrix}^T \end{aligned} \tag{1}$$

where $N_{1Be}=N_{1B}-N_{2B}/\gamma$ with $\gamma=h_2/h_1$. b is the width of the beam, E is the Young's modulus, M_{1B} and M_{2B} are the two bending moments at the crack tip B, and N_{1B} and N_{2B} are the axial forces at the crack tip B. The superscript R denotes rigid interfaces, and the other symbols have their usual meanings. G^R is of quadratic form in terms of M_{1B}, M_{2B} and N_{1Be} with coefficient matrix $[C]$ which is given in full in Appendix A. It is the same for the Euler and Timoshenko beam theories, and for 2D elasticity theory. However, its mode I and II partitions are different. In Euler beam theory, the partitions are

$$G_{IE}^{R}=c_{IE}\left(M_{1B}-\frac{M_{2B}}{\beta_1}-\frac{N_{1Be}}{\beta_2}\right)\left(M_{1B}-\frac{M_{2B}}{\beta_1'}-\frac{N_{1Be}}{\beta_2'}\right) \tag{2}$$

$$G_{IIE}^{R}=c_{IIE}\left(M_{1B}-\frac{M_{2B}}{\theta_1}-\frac{N_{1Be}}{\theta_2}\right)\left(M_{1B}-\frac{M_{2B}}{\theta_1'}-\frac{N_{1Be}}{\theta_2'}\right) \tag{3}$$

In Timoshenko beam theory, the partitions are

$$G_{IT}^{R}=c_{IT}\left(M_{1B}-\frac{M_{2B}}{\beta_1}-\frac{N_{1Be}}{\beta_2}\right)^2 \tag{4}$$

$$G_{IIT}^{R}=c_{IIT}\left(M_{1B}-\frac{M_{2B}}{\theta_1}-\frac{N_{1Be}}{\theta_2}\right)^2 \tag{5}$$

In the above equations

$$\theta_1=-\gamma^2,\ \theta_2=-\frac{6}{h_1},\ \beta_1=\frac{\gamma^2(3+\gamma)}{1+3\gamma},\ \beta_2=\frac{2(3+\gamma)}{h_1(\gamma-1)}\ \text{for}\ \gamma\neq 1,\ \beta_2=\infty\ \text{for}\ \gamma=1 \tag{6}$$

$$\theta_1'=-1,\ \theta_2'=-\frac{6(1+\gamma)}{h_1(1+\gamma^3)},\ \beta_1'=\gamma^3,\ \beta_2'=\infty \tag{7}$$

$$c_{IE}=G_{\theta_1}\left[\left(1-\frac{\theta_1}{\beta_1}\right)\left(1-\frac{\theta_1}{\beta_1'}\right)\right]^{-1},\ c_{IIE}=G_{\beta_1}\left[\left(1-\frac{\beta_1}{\theta_1}\right)\left(1-\frac{\beta_1}{\theta_1'}\right)\right]^{-1} \tag{8}$$

$$c_{IT}=G_{\theta_1}\left(1-\frac{\theta_1}{\beta_1}\right)^{-2},\ c_{IIT}=G_{\beta_1}\left(1-\frac{\beta_1}{\theta_1}\right)^{-2} \tag{9}$$

$$G_{\theta_1}=\frac{24\gamma}{Eb^2h_1^3(1+\gamma)},\ G_{\beta_1}=\frac{72\gamma(1+\gamma)}{Eb^2h_1^3(1+3\gamma)^2} \tag{10}$$

In Euler beam theory, the θ and β set of modes form the first set of orthogonal pure modes, giving pure mode I and II, respectively. For example, when $M_{2B}=\theta_1 M_{1B}$ and $N_{1Be}=0$, pure mode I occurs as the relative shearing displacement just behind the crack tip is zero. This pure mode I is denoted by θ_1. Its orthogonal pure mode II is β_1 which corresponds to zero crack tip opening force. Here, the 'orthogonal' means

$$\{1\quad \theta_1\quad 0\}[C]\{1\quad \beta_1\quad 0\}^T=0 \tag{11}$$

For simplicity, Eq. (11) can be written as $\theta_1=\text{orthogonal}(\beta_1)$. The θ' and β' set of modes form the second set of orthogonal pure modes, giving pure mode I and II respectively. For example, when $M_{2B}=\theta_1' M_{1B}$ and $N_{1Be}=0$, pure mode I occurs as the crack tip shearing force is zero. This pure mode I is denoted by θ_1'. Its orthogonal pure mode II is β_1', which corresponds to zero crack tip opening displacement. Details of derivations of the two sets of orthogonal pure modes can be found in Refs. [31,33]. An important feature of the pure modes from Euler beam theory is that the two sets of pure modes do not necessarily coincide. That is, for example, the θ_1 pure mode I corresponds to zero relative shearing displacement but with non-zero crack tip shearing stress. The β_1 pure mode II corresponds to zero opening crack tip stress but with non-zero crack

tip relative opening displacement. These characteristics arise from the rigidity of the interfaces and result in 'stealthy interaction' [31,33] between the θ pure mode I modes and the β pure mode II modes. Eq. (11) shows that the interaction between the θ_1 pure mode I and the β_1 pure mode II produces zero net ERR due to their orthogonality. However, this does not mean there is no interaction between them. In fact, interactions do exist within the context of Euler beam theory. The crack tip opening stress in the θ_1 pure mode I does work on the non-zero opening displacement in the β_1 pure mode II while the non-zero crack tip shearing stress in the θ_1 pure mode I does work on the shearing displacement in the β_1 pure mode II. The interactions change the mode I and II ERR partitions and are called 'stealthy interactions' in Refs. [31,33] as they produce zero net ERR. In Timoshenko beam theory these two sets of modes coincide on the first set resulting in no stealthy interaction. An approximate partition theory based on 2D elasticity is given by averaging the Euler and Timoshenko partitions [31,33]. It is worth noting that when ERR is calculated using the whole Δa-length crack influence zone, numerical simulations show that Euler beam, Timoshenko beam and 2D elasticity partitions are the same as that of Euler beam partitions in Eqs. (2) and (3). Hence, the Euler beam partitions are also called global partitions. Ref. [33] shows that the global partitions agree very well with experimental results.

It is important to note that the orthogonal property demonstrated in Eq. (11) exists between any pure mode pairs in the first set of pure modes (which consists of the θ and β pure modes). That is, $\theta_1 = \text{orthogonal}(\beta_1 \text{ or } \beta_2)$ and $\theta_2 = \text{orthogonal}(\beta_1 \text{ or } \beta_2)$. This property also applies to any pairs of the θ' and β' set. As long as one pure mode is known, say θ_1, the others can be obtained by using the orthogonal properties. This knowledge provides a powerful methodology to find pure modes and partition mixed modes which will be used in the following development.

2.2. Mixed-mode partitioning with non-rigid cohesive interfaces in Euler beam theory

From Fig. 1, the differential equations of beams 1 and 2 in the Δa region can be written as

$$EA_{1,2}u_{1,2}^{(1)} = N_{1,2B} \mp b\int_0^x \tau_s dx \tag{12}$$

$$EI_{1,2}w_{1,2}^{(2)} = \mp b\int_0^x\int_0^x \sigma_n dxdx - \frac{bh_{1,2}}{2}\int_0^x \tau_s dx + P_{1,2B}x + M_{1,2B} \tag{13}$$

where u and w are the respective axial and vertical displacements, $u^{(1)} = du/dx$ and $w^{(2)} = d^2w/dx^2$. The subscripts 1 and 2 indicate beams 1 and 2, which are the upper and lower beams respectively.

Note that in Eqs. (12) and (13), the origin of x is at point B and towards left. The relative shearing displacement at interface is defined as

$$\bar{u} = \bar{u}_2 - \bar{u}_1 = \left(u_2 - \frac{h_2}{2}w_2^{(1)}\right) - \left(u_1 + \frac{h_1}{2}w_1^{(1)}\right) \tag{14}$$

Positive $\bar{u}$ corresponds to positive interface shear stress τ_s which is determined using Eqs (12), (13) and (14).

$$\tau_s = \tau_{sP} + \tau_{s\sigma} + \tau_{s\bar{u}} \tag{15}$$

with

$$\tau_{sP} = \frac{3\left(\gamma^2 P_{1B} + P_{2B}\right)}{2bh_1\gamma(1+\gamma)} \tag{16}$$

$$\tau_{s\sigma} = \frac{3(1-\gamma)}{2h_1\gamma}\int_0^x \sigma_n dx \tag{17}$$

$$\tau_{s\bar{u}} = \frac{Eh_1\gamma\bar{u}^{(2)}}{4(1+\gamma)} \tag{18}$$

The mode II ERR can now be found using *J*-integral below.

$$\begin{aligned}
G_{IIE}^{NR} &= \lim_{da\to 0}\left\{\frac{1}{da}\int_0^{da}\int_0^{\bar{u}} \tau_s d\bar{u} dx\right\} \\
&= \int_0^{\bar{u}_B} \tau_{sB} d\bar{u}_B \\
&= \int_0^{\bar{u}_B} \tau_{sP} d\bar{u}_B + \int_0^{\bar{u}_B} \tau_{s\sigma B} d\bar{u}_B + \int_0^{\bar{u}_B} \tau_{s\bar{u}B} d\bar{u}_B \\
&= \int_0^{\bar{u}_B} \tau_{sP} d\bar{u}_B + \int_0^{\bar{u}_B} \frac{Eh_1\gamma}{4(1+\gamma)} \bar{u}_B^{(1)} d\bar{u}_B^{(1)} \\
&= \int_0^{\bar{u}_B} \tau_{sP} d\bar{u}_B + \frac{Eh_1\gamma}{8(1+\gamma)}\left\{\left[\bar{u}_B^{(1)}(\bar{u}_B)\right]^2 - \left[\bar{u}_B^{(1)}(0)\right]^2\right\} \\
&= \int_0^{\bar{u}_B} \tau_{sP} d\bar{u}_B + \frac{Eh_1\gamma}{8(1+\gamma)}\left(\bar{u}_B^{(1)}\right)^2 \\
&= G_{IIE}^{P} + G_{IIE}^{MN}
\end{aligned} \tag{19}$$

The superscript *NR* denotes non-rigid cohesive interfaces. The superscript *MN* denotes that the ERR G_{IIE}^{MN} is due to the crack tip bending moments and axial forces and the superscript *P* denotes that G_{IIE}^{P} is due to the crack tip shear forces. Also note that the following points were used in the derivation of Eq. (19): (1) since there is no stress singularity at the crack tip for a non-rigid cohesive interface, the crack tip shear stress $\tau_{s\sigma B} = 0$; (2) when the crack tip relative shearing displacement $\bar{u}_B = 0$, the crack tip relative shearing strain is also zero, i.e. $\bar{u}_B^{(1)}(0) = 0$; and (3) the crack tip relative shearing strain $\bar{u}_B^{(1)}(\bar{u}_B)$ in the second term of Eq. (19) is found from Eq. (14) to be

$$\begin{aligned}
\bar{u}_B^{(1)} &= -\frac{N_{1B}}{EA_1} + \frac{N_{2B}}{EA_2} - \frac{h_1 M_{1B}}{2EI_1} - \frac{h_2 M_{2B}}{2EI_2} \\
&= -\frac{6\gamma^2 M_{1B} + 6M_{2B} + \gamma^2 h_1^2 N_{1Be}}{Ebh_1^2\gamma^2}
\end{aligned} \tag{20}$$

It is easy to show that G_{IIE}^{MN} in Eq. (19) is equal to the ERR from the β_1 and β_2 modes for a rigid interface without any stealthy interaction [31,33]. That is, it is equal to the mode II ERR in Eq. (5) based on Timoshenko beam theory [31,33] or $G_{IIE}^{MN} = G_{IIT}^{R}$. Note that G_{IIE}^{MN} is independent of the interface constitutive law. The first term in Eq. (19), i.e. G_{IIE}^{P}, is from the β_1 mode of shear force and is determined below. Since the final ERR is independent of the order of application of τ_{sP} and $\tau_{s\bar{u}}$ in the case of non-rigid elastic interfaces, it can be assumed that τ_{sP} is applied first and then $\tau_{s\bar{u}}$ is applied afterwards. That is, the two crack tip shear forces P_{1B} and P_{2B} are applied first, then the two crack tip bending moments M_{1B} and M_{2B}, and the crack tip axial force N_{1Be} are applied afterwards. The first term in Eq. (19) can then be calculated as

$$G_{IIE}^{P} = \int_0^{\bar{u}_B} \tau_{sP} d\bar{u}_B = \int_0^{\bar{u}_{B\tau_{sP}}} \tau_{sB} d\bar{u}_B + \int_{\bar{u}_{B\tau_{sP}}}^{\bar{u}_{B\tau_{sP}}+\bar{u}_{B\tau_{s\bar{u}}}} \tau_{sP} d\bar{u}_B$$
$$= \int_0^{\bar{u}_{B\tau_{sP}}} \tau_{sB} d\bar{u}_B + \tau_{sP} \bar{u}_{B\tau_{s\bar{u}}} \tag{21}$$

By using a given interface constitutive law and τ_{sP} in Eq. (16), the interface relative shearing displacement $\bar{u}_{B\tau_{sP}}$ due to τ_{sP} is easily calculated and the first term in Eq. (21) is then determined. $\bar{u}_{B\tau_{s\bar{u}}}$ due to $\tau_{s\bar{u}}$ can be determined from

$$G_{IIE}^{MN} = \int_{\bar{u}_{B\tau_{sP}}}^{\bar{u}_{B\tau_{sP}}+\bar{u}_{B\tau_{s\bar{u}}}} \tau_{s\bar{u}B} d\bar{u}_B = \int_{\bar{u}_{B\tau_{sP}}}^{\bar{u}_{B\tau_{sP}}+\bar{u}_{B\tau_{s\bar{u}}}} \left(\tau_{sB} - \tau_{sP}\right) d\bar{u}_B \tag{22}$$

for a given interface constitutive law where G_{IIE}^{MN} is given in Eq. (19). In the case of non-rigid plastic interfaces, such as those described by bi-linear or exponential interface constitutive laws, the shear stress τ_{sP} is generally a very small fraction of the fracture initiation shear stress value, and the above approach is still applicable. Eq. (19) gives a complete analytical solution of mode II ERR for non-rigid cohesive interfaces which is explicitly independent of the size of the Δa-length crack influence zone.

The pure mode I condition can be obtained by letting $G_{IIE} = 0$. This results in both $\bar{u}_B^{(1)} = 0$ and $\tau_{sP} = 0$, which are the conditions for the pure mode I θ modes in Eq. (5) for a rigid interface [31,33]. For non-rigid cohesive interfaces, the condition $\bar{u}_B^{(1)} = 0$ nullifies the contribution of the shear stress $\tau_{s\bar{u}B}$ to the ERR. That is, $\tau_{s\bar{u}B}$ is effectively zeroed. However, note that $\tau_{s\bar{u}B} = 0$ leads to $\bar{u}_B^{(2)} = 0$ instead of $\bar{u}_B^{(1)} = 0$. In addition, the shear stress $\tau_{s\sigma B}$ is always zero for non-rigid cohesive interfaces. Therefore, for non-rigid cohesive interfaces both shear stress and strain at the crack tip are zero for pure mode I. The two sets of mode I θ modes and θ' modes in Eq. (3) coincide on the θ modes [31,33]. Consequently, the two sets of mode II β modes and β' modes in Eq. (2) should also coincide on the β modes [31,33]. There will be no stealthy interactions between the mode I θ set and mode II β set [31,33], which shows that it is the singularity shear stress $\tau_{s\sigma}$ in Eq. (17) at the crack tip for a rigid interface that causes stealthy interactions.

Next, mode I ERR G_{IE}^{NR} is considered. The relative opening displacement at interface is defined as

$$\bar{w} = \bar{w}_1 - \bar{w}_2 \tag{23}$$

Positive $\bar{w}$ corresponds to positive interface normal stress σ_n, which is found from Eqs (12), (13), (15) and (23) and given by Eq. (24).

$$\sigma_n = -\frac{E h_1^3 \gamma^3}{3(1+\gamma)^3}\left[\bar{w}^{(4)} + \frac{3(1-\gamma)}{2h_1\gamma}\bar{u}^{(3)}\right] \tag{24}$$

The mode I ERR is found by using *J*-integral.

$$G_{IE}^{NR} = \lim_{da\to 0}\left\{\frac{1}{da}\int_0^{da}\int_0^{\bar{w}} \sigma_n d\bar{w} dx\right\} = \int_0^{\bar{w}_B} \sigma_{nB} d\bar{w}_B \tag{25}$$

The following integrals are required to evaluate G_{IE}^{NR}:

$$
\begin{aligned}
\int_0^{\overline{w}_B} \overline{w}_B^{(4)} d\overline{w}_B &= \int_0^{\overline{w}_B} \overline{w}_B^{(1)} d\overline{w}_B^{(3)} \\
&= \overline{w}_B^{(1)}\left(\overline{w}_B\right)\overline{w}_B^{(3)}\left(\overline{w}_B\right) - \overline{w}_B^{(1)}(0)\overline{w}_B^{(3)}(0) - \int_0^{\overline{w}_B} \overline{w}_B^{(2)} d\overline{w}_B^{(2)} \\
&= \overline{w}_B^{(1)}\left(\overline{w}_B\right)\overline{w}_B^{(3)}\left(\overline{w}_B\right) - \left[\overline{w}_B^{(2)}\right]^2 / 2 \\
&= \frac{12\left(\gamma^3 P_{1B} - P_{2B}\right)}{Eb\gamma^3 h_1^3}\overline{w}_B^{(1)} - \frac{72\left(\gamma^3 M_{1B} - M_{2B}\right)^2}{\left(Eb\gamma^3 h_1^3\right)^2}
\end{aligned}
\tag{26}
$$

$$
\begin{aligned}
\int_0^{\overline{w}_B} \overline{u}_B^{(3)} d\overline{w}_B &= \int_0^{\overline{w}_B} \overline{w}_B^{(1)} d\overline{u}_B^{(2)} \\
&= \overline{w}_B^{(1)}\left(\overline{w}_B\right)\overline{u}_B^{(2)}\left(\overline{w}_B\right) - \overline{w}_B^{(1)}(0)\overline{u}_B^{(2)}(0) - \int_0^{\overline{w}_B} \overline{u}_B^{(2)} d\overline{w}_B^{(1)} \\
&= \overline{w}_B^{(1)}\left(\overline{w}_B\right)\overline{u}_B^{(2)}\left(\overline{w}_B\right) - \int_0^{\overline{w}_B} \overline{u}_B^{(2)} d\overline{w}_B^{(1)}
\end{aligned}
\tag{27}
$$

As seen earlier, the shear stress $\tau_{s\bar{u}}$ at crack tip is effectively zero in mode I leading to $\overline{u}_B^{(2)} = 0$ from Eq. (18). Therefore, Eq. (27) becomes zero. Moreover, it is therefore the mode I θ modes [31,33] that produce the G_{IE}^{NR}. Any given P_{1B} and P_{2B} in question can be decomposed by [31,33].

$$
\begin{Bmatrix} P_{1B} \\ P_{2B} \end{Bmatrix} = \begin{bmatrix} 1 & 1 \\ \theta_1 & \beta_1 \end{bmatrix} \begin{Bmatrix} \alpha_{\theta_1} \\ \alpha_{\beta_1} \end{Bmatrix}
\tag{28}
$$

where θ_1 and β_1 are given in Eq. (6). α_{θ_1} and α_{β_1} are mode partition coefficients and are determined from Eq. (28) as

$$
\begin{Bmatrix} \alpha_{\theta_1} \\ \alpha_{\beta_1} \end{Bmatrix} = \frac{1}{\beta_1 - \theta_1} \begin{Bmatrix} \beta_1 P_{1B} - P_{2B} \\ -\theta_1 P_{1B} + P_{2B} \end{Bmatrix}
\tag{29}
$$

Any given M_{1B}, M_{2B} and N_{1Be} can be decomposed by [31,33]

$$
\begin{Bmatrix} M_{1B} \\ M_{2B} \\ N_{1Be} \end{Bmatrix} = \begin{bmatrix} 1 & 1 & 1 \\ \theta_1 & \beta_1 & 0 \\ 0 & 0 & \beta_2 \end{bmatrix} \begin{Bmatrix} \alpha_{\theta_1} \\ \alpha_{\beta_1} \\ \alpha_{\beta_2} \end{Bmatrix}
\tag{30}
$$

From Eq. (30), the partition coefficients are given by

$$
\alpha_{\beta_2} = \frac{N_{1Be}}{\beta_2} \quad \text{and} \quad \begin{Bmatrix} \alpha_{\theta_1} \\ \alpha_{\beta_1} \end{Bmatrix} = \frac{1}{\beta_1 - \theta_1} \begin{Bmatrix} \beta_1\left(M_{1B} - \alpha_{\beta_2}\right) - M_{2B} \\ -\theta_1\left(M_{1B} - \alpha_{\beta_2}\right) + M_{2B} \end{Bmatrix}
\tag{31}
$$

Substituting the θ_1 mode I component given in Eq. (28) for shear forces and the θ_1 mode I components given in Eq. (31) for bending moments into Eq. (26) gives

$$
\int_0^{\overline{w}_B} \overline{w}_B^{(4)} d\overline{w}_B = \frac{3(1+3\gamma)\left(\beta_1 P_{1B} - P_{2B}\right)}{Eb\gamma^3 h_1^3}\overline{w}_B^{(1)} - \frac{72\alpha_{\theta_1}^2 \gamma^4 (1+\gamma)^2}{\left(Eb\gamma^3 h_1^3\right)^2}
\tag{32}
$$

Substituting Eq. (32) into Eq. (25) gives

$$
\begin{aligned}
G_{IE}^{NR} &= G_{IE}^{MN} + \frac{(1+3\gamma)(P_{2B} - \beta_1 P_{1B})}{b(1+\gamma)^3}\overline{w}_B^{(1)} \\
&= G_{IE}^{MN} - \frac{F_n}{b}\overline{w}_B^{(1)} \\
&= G_{IE}^{MN} + G_{IE}^{P}
\end{aligned} \tag{33}
$$

The first term $G_{IE}^{MN} = \alpha_{\theta_1}^2 G_{\theta_1} = 24\alpha_{\theta_1}^2 \gamma \big/ \left[(1+\gamma)Eb^2 h_1^3\right]$ in Eq. (33) is equal to the ERR from the θ_1 mode for rigid interfaces [31,33], where α_{θ_1} is given in Eq. (31). It is easy to show that G_{IE}^{MN} is the same as the mode I ERR for a rigid interface in Eq. (4) based on Timoshenko beam theory [31,33] or $G_{IE}^{MN} = G_{IT}^{R}$. Note that G_{IE}^{MN} is also independent of interface constitutive law. The $\overline{w}_B^{(1)}$ in the second term of Eq. (33) is the relative crack tip rotation and F_n is the resultant normal force in the Δa-length crack influence zone which is defined as [31]

$$
F_n = b\int_0^{\Delta a} \sigma_n dx \tag{34}
$$

It is seen that Eq. (33) is not completely analytical due to the second term G_{IE}^{P}, which arises from crack tip shear forces. However, it can be neglected for most practical engineering applications which have non-rigid but hard interfaces. There is no clear-cut definition of a hard interface, which can vary considerably from Euler and Timoshenko beam theory to 2D elasticity theory. Since interface constitutive laws are usually expressed in a linear, bi-linear or exponential form, a hard interface is indicated in this work by the ratios between penalty stiffnesses k_σ (for opening stress σ_n) and k_τ (for shear stress τ_s), and the Young's modulus E of the DCB material. Some more specific details will be given in the examples in the numerical test sections for both the beam theories (in Section 3) and 2D elasticity theory (in Section 4).

2.3. Mixed-mode partitioning with non-rigid cohesive interfaces in Timoshenko beam theory

Using the Timoshenko beam theory, the governing equations become

$$
EA_{1,2}u_{1,2}^{(1)} = N_{1,2B} \mp b\int_0^x \tau_s dx \tag{35}
$$

$$
EI_{1,2}\psi_{1,2}^{(1)} = \mp b\int_0^x\int_0^x \sigma_n dx dx - \frac{bh_{1,2}}{2}\int_0^x \tau_s dx + P_{1,2B}x + M_{1,2B} \tag{36}
$$

$$
k^2 G_{xz}A_{1,2}\left(w_{1,2}^{(1)} - \psi_{1,2}\right) = -P_{1,2B} \pm b\int_0^x \sigma_n dx \tag{37}
$$

where G_{xz} is the through thickness shear modulus, k^2 is the shear correction factor, usually taken to be 5/6 for isotropic materials with a rectangular cross-section and ψ is the cross-sectional rotation, which is positive in the clockwise direction. Note that the shear correction factor k^2 is introduced to make a mechanical correction for the uniform through-thickness shear strain that is assumed in the theory. It is simple to verify that the mode II ERR G_{IIT}^{NR} remains the same as the G_{IIE}^{NR} in Eq. (19). This is because the interface shear stress τ_s from Euler beam theory, given in Eqs. (15) to (18), remains unchanged when Timoshenko beam theory is used instead. This is most easily seen by replacing $w_{1,2}^{(2)}$ in Eq.(13) with $\psi_{1,2}^{(1)}$, and replacing $w_{1,2}^{(1)}$ in Eq. (13) with $\psi_{1,2}$. Since Eq. (12) remains unchanged, the two beam theories therefore give the same

expression for τ_s. However, the mode I ERR G_{IT}^{NR} needs reconsideration. From the above three equations, the governing equation for the interface normal stress σ_n is found.

$$\sigma_n^{(2)} - \lambda^2 \sigma_n = \alpha\left(\overline{w}^{(4)} + \frac{3(1-\gamma)}{2h_1\gamma}\overline{u}^{(3)} \right) \tag{38}$$

where $\lambda = (1+\gamma)\left(3k^2 G_{xz}/E\right)^{1/2}/(\gamma h_1)$ and $\alpha = k^2 G_{xz} h_1 \gamma/(1+\gamma)$. By using the method of parameter variation, the solution to Eq. (38) is found.

$$\begin{aligned}\sigma_n = {} & c_1 e^{\lambda x} + c_2 e^{-\lambda x} + \alpha\left[\lambda^2 \overline{w} + \overline{w}^{(2)} + \frac{3\overline{u}^{(1)}(1-\gamma)}{2h_1\gamma} \right] \\ & + \frac{\alpha\lambda^3}{2}\left(e^{\lambda x}\int_0^x \overline{w} e^{-\lambda x} dx - e^{-\lambda x}\int_0^x \overline{w} e^{\lambda x} dx \right) \\ & + \frac{3\alpha\lambda^2(1-\gamma)}{4h_1\gamma}\left(e^{\lambda x}\int_0^x \overline{u} e^{-\lambda x} dx + e^{-\lambda x}\int_0^x \overline{u} e^{\lambda x} dx \right)\end{aligned} \tag{39}$$

The two integration constants c_1 and c_2 are determined using the conditions $\sigma_n(\Delta a) = \sigma_n^{(1)}(\Delta a) = 0$.

$$c_1 = -\frac{\alpha\lambda^3}{2}\int_0^{\Delta a} \overline{w} e^{-\lambda x} dx - \frac{3\alpha\lambda^2(1-\gamma)}{4h_1\gamma}\int_0^{\Delta a} \overline{u} e^{-\lambda x} dx \tag{40}$$

$$c_2 = \frac{\alpha\lambda^3}{2}\int_0^{\Delta a} \overline{w} e^{\lambda x} dx - \frac{3\alpha\lambda^2(1-\gamma)}{4h_1\gamma}\int_0^{\Delta a} \overline{u} e^{\lambda x} dx \tag{41}$$

Then, mode I ERR is found using *J*-integral.

$$\begin{aligned} G_{IT}^{NR} &= \lim_{da\to 0}\left\{ \frac{1}{da}\int_0^{da}\int_0^{\overline{w}} \sigma_n d\overline{w} dx \right\} \\ &= \int_0^{\overline{w}_B} \sigma_{nB} d\overline{w}_B \\ &= \int_0^{\overline{w}_B} (c_1 + c_2) d\overline{w}_B + \frac{\alpha\lambda^2}{2}\overline{w}_B^2 + \frac{\alpha}{2}\left(\overline{w}_B^{(1)}\right)^2 + \frac{3\alpha(1-\gamma)}{2h_1\gamma}\int_0^{\overline{w}_B} \overline{u}_B^{(1)} d\overline{w}_B \end{aligned} \tag{42}$$

The two integral constants c_1 and c_2 are determined in what follows. The resultant normal force F_n is defined in Eq. (34) and the resultant moment M_n in the Δa-length crack influence zone is defined as [31]

$$M_n = b\int_0^{\Delta a}\int_0^x \sigma_n dx dx = b\int_0^{\Delta a} \sigma_n(\Delta a - x) dx = M_{nm} + F_n \Delta a \tag{43}$$

where

$$F_n = \frac{1+3\gamma}{(1+\gamma)^3}\left(\beta_1 P_{1B} - P_{2B}\right) \tag{44}$$

when transverse shear stress is calculated through equilibrium consideration with the bending stress, or

$$F_n = \frac{1}{1+\gamma}\left(\gamma P_{1B} - P_{2B}\right) \tag{45}$$

when transverse shear stress is through the constitutive law, and

$$M_{nm} = \frac{1+3\gamma}{(1+\gamma)^3}\left(\beta_1 M_{1B} - M_{2B}\right) + \frac{h_1\gamma^2(1-\gamma)}{2(1+\gamma)^3} N_{1Be} \tag{46}$$

Substituting σ_n in Eq. (39) into Eqs. (34) and (43) gives

$$c_1 - c_2 = -\lambda\left\{\alpha\left[\overline{w}_B^{(1)} + \frac{3(1-\gamma)}{2h_1\gamma}\overline{u}_B\right] + \frac{F_n}{b}\right\} \tag{47}$$

and

$$c_1 + c_2 = -\lambda^2\left(\alpha\overline{w}_B + M_{nm}/b\right) \tag{48}$$

Substituting Eq. (48) into Eq. (42) gives

$$\begin{aligned} G_{IT}^{NR} &= -\int_0^{\overline{w}_B} \frac{\lambda^2 M_{nm}}{b} d\overline{w}_B + \frac{\alpha\left(\overline{w}_B^{(1)}\right)^2}{2} + \frac{3\alpha(1-\gamma)}{2h_1\gamma}\int_0^{\overline{w}_B} \overline{u}_B^{(1)} d\overline{w}_B \\ &= \int_0^{\overline{w}_{B\sigma_I}} \sigma_I d\overline{w}_B + \sigma_I\left(\overline{w}_B - \overline{w}_{B\sigma_I}\right) + \alpha\left(\overline{w}_B^{(1)}\right)^2/2 \end{aligned} \tag{49}$$

Note that the first term in Eq. (49) is calculated from a given interface constitutive law with $\sigma_I = -\lambda^2 M_{nm}/b + \left[3\alpha(1-\gamma)/(2h_1\gamma)\right]\overline{u}_B^{(1)}$ in which M_{nm} and $\overline{u}_B^{(1)}$ are given in Eqs. (46) and (20) respectively. $\overline{w}_B$ and $\overline{w}_B^{(1)}$ need to be determined numerically. It is easy to show that for a rigid interface the first two terms in Eq. (49) are zero and the third term becomes

$$G_{IT}^R = \alpha_{\theta_1}^2 G_{\theta_1} + G_P + \alpha_{\theta_1}\Delta G_{\theta_1 P} \tag{50}$$

as given in [31]. Note that the first term in G_{IT}^R in Eq. (50) is the ERR contribution from the crack tip bending moments and axial forces, which is same as that in Eq. (4); the second and third terms are from crack tip shear forces. For most of practical engineering problems with hard interfaces the third term in Eq. (49) can be replaced by G_{IT}^R in Eq. (50). Therefore, $\overline{w}_B$ in the second term of Eq. (49) can be calculated by using a given interface constitutive law and the following:

$$G_{IT}^R = \int_{\overline{w}_{B\sigma_I}}^{\overline{w}_B} \left(\sigma_{nB} - \sigma_I\right) d\overline{w}_B \tag{51}$$

The mode I ERR G_{IT}^{NR} for a hard interface is then obtained analytically. Again, the ERR G_{IT}^{NR} in Eq. (49) is explicitly independent of the size of the crack influence zone Δa.

2.4. Mixed-mode partitioning with non-rigid cohesive interfaces in 2D elasticity theory

When the upper and lower beams are modelled using 2D elasticity theory, the total ERR can in general still be written in the form

$$G_{2D}^{NR} = G_{2D}^{MN} + G_{2D}^{P} = G_{I2D}^{MN} + G_{II2D}^{MN} + G_{I2D}^{P} + G_{II2D}^{P} \tag{52}$$

Moreover, it is expected that

$$G_{2D}^{MN} = G_{IE}^{MN} + G_{IIE}^{MN} \tag{53}$$

should be a good approximation for non-rigid hard interfaces. The aim in the following is to partition G_{2D}^{NR} in Eq. (52). Based on the authors' previous work [33] and also the above developments based on beam theories, the partition of G_{2D}^{MN} can be written in a form similar to that in Eqs. (4) and (5), as follows:

$$G_{I2D}^{MN} = c_I\left(M_{1B} - \frac{M_{2B}}{\beta_{1NR}} - \frac{N_{1Be}}{\beta_{2NR}} \right)^2,\ G_{II2D}^{MN} = c_{II}\left(M_{1B} - \frac{M_{2B}}{\theta_{1NR}} - \frac{N_{1Be}}{\theta_{2NR}} \right)^2 \tag{54}$$

where

$$c_I = G_{\theta_{1NR}}\left(1 - \frac{\theta_{1NR}}{\beta_{1NR}}\right)^{-2},\ c_{II} = G_{\beta_{1NR}}\left(1 - \frac{\beta_{1NR}}{\theta_{1NR}}\right)^{-2} \tag{55}$$

$$G_{\theta_{1NR}} = \frac{1}{2Eb}\left(\frac{1}{I_1} + \frac{\theta_{1NR}^2}{I_2} - \frac{\left(1+\theta_{1NR}\right)^2}{I}\right),\ G_{\beta_{1NR}} = \frac{1}{2Eb}\left(\frac{1}{I_1} + \frac{\beta_{1NR}^2}{I_2} - \frac{\left(1+\beta_{1NR}\right)^2}{I}\right) \tag{56}$$

θ_{1NR} and θ_{2NR} are two pure mode I modes. β_{1NR} and β_{2NR} are two pure mode II modes. In the following development, interface constitutive laws with an initial linear elastic part and then either a linear or non-linear softening part are assumed. With these types of interface constitutive law, numerical simulations show that these pure modes are dependent on the ratio of the interface penalty stiffness to the Young's modulus, that is, they are dependent on $k_{er\sigma} = k_\sigma / E$ and $k_{er\tau} = k_\tau / E$. In the following analytical development, it is assumed that $k_{er\sigma} = k_{er\tau} = k_{er}$. The effect of the assumption will be investigated by numerical simulations in Section 4.2. As noted in Section 2.1, the authors' previous work [31,33] provides a powerful methodology to determine these pure modes, that is, the orthogonal methodology. If any one of the four pure modes is known, the other three can be determined by using the orthogonal property between them. This methodology is again used here. θ_{1NR} is found first and then θ_{2NR}, β_{1NR} and β_{2NR} are determined using the orthogonal methodology.

In the authors' previous work [31,33], an averaged partition theory has been developed for mixed-mode partitioning with rigid interfaces in 2D elasticity, details of which are given in Refs. [31,33]. It has been found that the pure mode I θ_{1H} in the averaged theory [31,33] and Suo and Hutchinson's [3] partition theory are between the pure mode I θ_1 and θ_1' modes in the mixed-mode partition theory based on Euler beam theory. It is expected that for a non-rigid cohesive interface, the pure mode I θ_{1NR} mode based on 2D elasticity is between the pure mode I θ_{1H} and θ_1' modes and dependent of the interface stiffness. The following approximate relationships are found based on numerical results:

$$\theta_{1NR}(\gamma, k_{er}) = \theta_{1NR}(\gamma, 10) = \theta_a(\gamma) = \frac{1}{4}(\theta_1 + 3\theta_1') \tag{57}$$

$$\theta_{1NR}(\gamma, k_{er}) = \theta_{1NR}(\gamma, 1) = \theta_b(\gamma) = \frac{1}{2}(\theta_a + \theta_c) \tag{58}$$

$$\theta_{1NR}(\gamma, k_{er}) = \theta_{1NR}(\gamma, 0.1) = \theta_c(\gamma) = \text{orthogonal}(\beta_c) \tag{59}$$

$$\beta_c(\gamma) = \frac{1}{4}(\beta_1 + 3\beta_1') \tag{60}$$

Note that the assumed units of k_{er} are m^{-1}. By using quadratic interpolation in terms of $\log_{10} k_{er}$ and θ_a, θ_b and θ_c, $\theta_{1NR}(\gamma, k_{er})$ is obtained and is given by Eq. (61).

$$\theta_{1NR}(\gamma, k_{er}) = \theta_b + 1/2(\theta_a - \theta_c)\log_{10} k_{er} + 1/2(\theta_a - 2\theta_b + \theta_c)(\log_{10} k_{er})^2 \tag{61}$$

Then θ_{2NR}, β_{1NR} and β_{2NR} are determined using the orthogonal methodology, that is

$$\theta_{2NR}(\gamma, k_{er}) = \text{orthogonal}(\beta_{1NR}) = \text{orthogonal}(\beta_{2NR}) \tag{62}$$

$$\beta_{1NR}(\gamma, k_{er}) = \text{orthogonal}(\theta_{1NR}) = \text{orthogonal}(\theta_{2NR}) \tag{63}$$

$$\beta_{2NR}(\gamma, k_{er}) = \text{orthogonal}(\theta_{1NR}) = \text{orthogonal}(\theta_{2NR}) \tag{64}$$

When k_{er} is inside the range from 0.1 to 10, the quartic approximation in Eq. (61) gives excellent agreement with FEM simulations. When it is outside of this range, higher order interpolations give better predictions by using θ_{1H} and θ_1' in addition to θ_a, θ_b and θ_c. Appendix B gives a good approximation using a cubic spline interpolation between these points. As noted earlier, G_{IE}^{MN} in Eq. (33) and G_{IIE}^{MN} in Eq. (19) are due to θ opening modes and β shearing modes respectively, which are independent of the interface constitutive laws. Hence, it is expected that θ_{1NR}, θ_{2NR}, β_{1NR} and β_{2NR} are also independent of the interface constitutive laws apart from k_{er}. Numerical simulations will demonstrate this important property.

Next, the partition of G_{2D}^P in Eq. (52) is considered. Its mode I component G_{I2D}^P is determined first. Based on the expression for G_{IE}^P in Eq. (33), G_{I2D}^P in the case of P_{1B} and P_{2B} acting alone is written in the following form for a given k_{er} ratio, thickness h_1 and un-cracked length L:

$$G_{IP}^P(\gamma) = \frac{\xi(\gamma)[P_{2B} - \beta_P(\gamma)P_{1B}]^2}{Eh_1^3} \tag{65}$$

where $\xi(\gamma)$ and $\beta_P(\gamma)$ are two γ-dependent parameters which can be determined numerically by consideration of two loading cases. The two cases chosen here are $P_{1B} = 1$, $P_{2B} = 0$ and $P_{1B} = 1$, $P_{2B} = -1$, giving

$$G_{IP,0}^P(\gamma) = \frac{\xi(\gamma)\beta_P^2(\gamma)}{Eh_1^3} \tag{66}$$

and

$$G_{IP,-1}^P(\gamma) = \frac{\xi(\gamma)[1 + \beta_P(\gamma)]^2}{Eh_1^3} \tag{67}$$

where $G_{IP,0}^P(\gamma)$ and $G_{IP,-1}^P(\gamma)$ are determined numerically. The two parameters $\xi(\gamma)$ and $\beta_P(\gamma)$ are therefore determined as

$$\xi(\gamma) = \left[\frac{G_{IP,0}^{NR}(\gamma)}{\beta_P^2(\gamma)}\right] Eh_1^3 \tag{68}$$

and

$$\beta_P(\gamma) = \left[g^{1/2}(\gamma) - 1\right]^{-1} \tag{69}$$

with $g(\gamma)=G_{IP,-1}^{NR}(\gamma)/G_{IP,0}^{NR}(\gamma)$. Appendix C gives approximate formulae for $\xi(\gamma)$ and $\beta_P(\gamma)$ based on fitting curves to results from FEM simulations. It is easy to show the following relationships:

$$\beta_P(1/\gamma)=1/\beta_P(\gamma) \tag{70}$$

$$\xi(1/\gamma)=\gamma^3\beta_P^2(\gamma)\xi(\gamma) \tag{71}$$

They are useful to avoid extra computations. Thus, $G_{IP}^{P}(\gamma)$ for any given crack tip shear forces P_{1B} and P_{2B} can be determined by using Eq. (65).

Now, consider G_{I2D}^{P} in a general loading condition. For a given interface constitutive law, the G_{IP}^{P} in Eq. (65) and G_{I2D}^{MN} in Eq. (52) can also be written as

$$G_{IP}^{P}=\int_0^{\overline{w}_{BP}}\sigma_{nBP}d\overline{w}_B \tag{72}$$

and

$$G_{I2D}^{MN}=\int_{\overline{w}_{BP}}^{\overline{w}_B}(\sigma_{nB}-\sigma_{nBP})d\overline{w}_B \tag{73}$$

Since G_{IP}^{P} and G_{I2D}^{MN} are known, both σ_{nBP} and $\overline{w}_{BP}$ can be found from Eq. (72) and $\overline{w}_B$ from Eq. (73). Therefore, the G_{I2D}^{P} in a general loading condition is now

$$G_{I2D}^{P}=G_{IP}^{P}+\sigma_{nBP}(\overline{w}_B-\overline{w}_{BP}) \tag{74}$$

The mode II component G_{II2D}^{P} in Eq. (52) is now considered. Similarly, based on Eq. (16), the crack tip shear stress τ_{sP} due to the shear forces P_{1B} and P_{2B} is written in the following form for given k_{er} ratio, thickness h_1 and un-cracked length L:

$$\tau_{sP}(\gamma)=\frac{\zeta(\gamma)[P_{2B}-\theta_P(\gamma)P_{1B}]}{bh_1} \tag{75}$$

where $\zeta(\gamma)$ and $\theta_P(\gamma)$ are two γ-dependent parameters and are determined numerically by consideration of two loading cases. The two cases chosen here are $P_{1B}=1$, $P_{2B}=0$ and $P_{1B}=1$, $P_{2B}=-1$, giving

$$\zeta(\gamma)=[\tau_{sP,0}(\gamma)-\tau_{sP,-1}(\gamma)]bh_1 \tag{76}$$

and

$$\theta_P(\gamma)=[\tau(\gamma)-1]^{-1} \tag{77}$$

with $\tau(\gamma)=\tau_{sP,-1}(\gamma)/\tau_{sP,0}(\gamma)$ determined numerically. Appendix C gives approximate formulae for $\zeta(\gamma)$ and $\theta_P(\gamma)$ based on fitting curves to results from FEM simulations. Similarly, it is easy to show the following relationships.

$$\theta_P(1/\gamma)=1/\theta_P(\gamma) \tag{78}$$

$$\zeta(1/\gamma)=-\gamma\theta_P(\gamma)\zeta(\gamma) \tag{79}$$

Therefore, in a similar way to Eq. (21), the ERR G_{II2D}^{P} is given by

$$G_{II\,2D}^{P} = \int_0^{\bar{u}_B} \tau_{sP} d\bar{u}_B = \int_0^{\bar{u}_{B\tau_{sP}}} \tau_{sB} d\bar{u}_B + \int_{\bar{u}_{B\tau_{sP}}}^{\bar{u}_B} \tau_{sP} d\bar{u}_B$$
$$= \int_0^{\bar{u}_{B\tau_{sP}}} \tau_{sB} d\bar{u}_B + \tau_{sP}\left(\bar{u}_B - \bar{u}_{B\tau_{sP}}\right) \tag{80}$$

For a given interface constitutive law, the first term in Eq. (80) is readily obtained and $\bar{u}_{B\tau_{sP}}$ is also known. The $\bar{u}_B$ in the second term in Eq. (80) can be obtained by using

$$G_{II\,2D}^{MN} = \int_{\bar{u}_{B\tau_{sP}}}^{\bar{u}_B} \left(\tau_{sB} - \tau_{sP}\right) d\bar{u}_B \tag{81}$$

3. Numerical tests with the beam partition theories

To validate the analytical beam partition theories, an FEM simulation capability has been developed based on Timoshenko beam theory and 2D elasticity. Interfaces are modelled with normal and shear point springs. Unless stated otherwise, ERR and its partitions are calculated by means of the crack closure technique, using the spring forces and relative displacements at the crack tip. Contact is not considered, although it has been dealt with in detail in previous work by the authors [31].

Two numerical tests were carried out on the DCB shown in Fig. 1a. As the Young's modulus E is merely a constant factor in the analysis it is assumed to be a unit value for simplicity, i.e. $E = 1\,\text{GPa}$. The Poisson's ratio is $\nu = 0.3$. The intact length is $L = 100\,\text{mm}$, the crack length is $a = 10\,\text{mm}$ and the width is $b = 1\,\text{mm}$. The total thickness is $h = h_1 + h_2 = 3\,\text{mm}$ with $h_1 = 1\,\text{mm}$. Therefore, the thickness ratio is $\gamma = h_2/h_1 = 2$. In each test, the DCB was either under tip bending moments $M_1 = 1\,\text{Nm}$ and M_2, which was varied from $-10\,\text{Nm}$ to $10\,\text{Nm}$, or under tip shear forces $P_1 = 1\,\text{kN}$ and P_2, which was also varied from $-10\,\text{kN}$ to $10\,\text{kN}$. In the first of the two numerical tests, linear Timoshenko beam elements with the very large shear modulus of $G_{xz} = 10^4\,\text{GPa}$ in comparison with the unit value of E were used to simulate Euler beam theory. The second test used linear Timoshenko beam elements but with the normal shear modulus of $G_{xz} = E/\left[2(1+\nu)\right] = 1/2.6\,\text{GPa}$.

All the finite element meshes, except for the ones marked as having 1310×2 elements (in the following tables), had uniform element density along the length and through the thickness. Details on these uniform meshes are given at appropriate points in the following discussion. In order to obtain accurate, mesh-independent partitions of ERR, the simulations with a rigid interface, linear Timoshenko beam elements and the normal value of shear modulus, and the simulations with a non-rigid elastic interface, linear Timoshenko beams and any value of shear modulus required a very fine mesh in the vicinity of the crack tip. For these cases, meshes with a total of 1310×2 elements were used. In the region of length 1.2 mm centered on the crack tip, 1200 elements with a length of 0.001 mm were uniformly distributed. In the remaining intact section of the DCB, 100 elements were uniformly distributed. In the remaining cracked section of the DCB, 10 elements were uniformly distributed.

3.1. Rigid interfaces with tip bending moments

The results for a rigid interface, with uniform interface spring stiffness $k_s = 10^6\,\text{kN/mm}$, are briefly presented because it is useful to compare the results from the non-rigid interfaces with them. The analytical theories for rigid interfaces have been presented in full detail by the authors in Refs. [31,33] and briefly in Section 2.1. The various analytical and numerical results are compared in Tables 1 and 2. Because the interface is rigid, the virtual crack closure technique was used to calculate ERR. The Timoshenko beam element simulations with the very large shear

modulus $G_{xz} = 10^4$ GPa very closely match the analytical Euler beam partition theory. Only 11×2 beam elements were needed for convergence with this close degree of agreement. When a normal shear modulus $G_{xz} = 1/2.6$ GPa was used, many more elements in the vicinity of the crack tip are required to obtain the same degree of agreement with the analytical Timoshenko beam partition theory. Nevertheless, when this is done, excellent agreement is observed, as shown by the results with the non-uniform mesh with 1310×2 elements. The 2D FEM results in this section are from four-node plane-stress quadrilateral (QUAD4) elements with full integration. The averaged partition rule for rigid interfaces [31,33] offers a good approximation to the 2D FEM results.

It is worth noting the following point: although the total ERR is non-negative definite, negative G_I and G_{II} can occur in the Euler beam partitions. This indicates that the corresponding crack tip force does negative work when closing the crack. This phenomenon arises from the stealthy interaction [31] which results in two sets of orthogonal pure modes as shown in Eqs. (2) and (3).

3.2. Linear elastic interfaces with tip bending moments

The present theories are applicable to general non-rigid elastic interfaces including both linear and non-linear ones, and non-rigid plastic interfaces with no unloading and crack closure. In this section, beams with two different linear elastic interfaces are considered. Interface constitutive laws relate the interface stresses to the relative displacements across the interface, i.e. $\sigma_n = k_\sigma \overline{w}$ and $\tau_s = k_\tau \overline{u}$ where k_σ and k_τ are the stiffness of the interface, which here are taken to be the same values for both opening and shearing action in the FEM simulations though different values can be used. Since the beam simulations use interface point springs, which relate the interface spring forces to the relative displacements, i.e. $F_{ns} = k_s \overline{w}$ and $F_{ss} = k_s \overline{u}$ where k_s is the spring stiffness, the stiffness of an individual interface spring force is therefore set to $k_s = b k_\sigma \delta a$ where δa is the spring pitch, i.e. the beam element length. It is usual to describe an interface as being hard or soft by comparing the interface stiffness k_σ with the Young's modulus E of the beam material. A hard interface has stiffness values k_σ which are expected to be around the order of E. However, the Young's modulus E in the thickness direction is effectively infinite in both Euler and Timoshenko beam theories. It was seen in Section 3.1 that a rigid interface is well represented with interface springs of stiffness $k_s = 10^6$ kN/mm which corresponds to an interface stiffness k_σ varying from around $k_\sigma = 10^5$ GPa/mm for $\delta a = 10$ mm to around $k_\sigma = 10^9$ GPa/mm for $\delta a = 10^{-3}$ mm. Therefore, it is reasonable to assume that a non-rigid hard interface can be represented by $k_\sigma = 10^3$ GPa/mm and $k_\sigma = 10^2$ GPa/mm. These two interfaces are considered in the following applications.

The results for the DCB with the $k_\sigma = 10^3$ GPa/mm linear elastic interface and tip bending moments $M_1 = 1$ Nm and M_2, which was varied from −10 Nm to 10 Nm, are presented in Tables 3 and 4. As shown by Eqs. (19) and (33), in this loading case and with the linear elastic interface, the analytical Euler beam partition results are the same as the analytical Timoshenko beam partition results with a rigid interface. There are no stealthy interactions and there is only one set of pure modes, which is the first set, i.e. $\theta_1 = -4$, $\beta_1 = 20/7$.

The analytical Timoshenko beam G_{II} partition is the same as the Euler beam G_{II} partition. However, as shown by Eq. (49), the analytical Timoshenko beam G_I partition depends on $\overline{w}_B$ and $\overline{w}_B^{(1)}$, which are in turn dependent on the interface constitutive law. These two quantities

could be determined from FEM simulations and used as arguments to Eq. (49). However, in the case of non-rigid hard interfaces, the third term in Eq. (49) can be replaced with Eq. (50), and Eq. (51) can be used to calculate $\overline{w}_B$. This gives a completely analytical expression. In this case, since there are no applied shear forces, the analytical Timoshenko beam partitions are very close to the Euler ones.

The Timoshenko beam element simulations with the very large shear modulus $G_{xz} = 10^4$ GPa converge slowly towards the analytical Euler beam partition theory. A large number of elements in the vicinity of the crack tip is required to obtain this good agreement. This is expected since point interface springs are more suited to capture the stress singularity at the crack tip that is observed for a rigid interface. The numerical results confirm that there is no stealthy interaction in Euler beam theory with a non-rigid elastic interface, and therefore there is a single set of pure modes which is given by $\theta_1 = -4$ and $\beta_1 = 20/7$. When Timoshenko beam elements with a normal shear modulus $G_{xz} = 1/2.6\,\text{GPa}$ are used, the results are very close to the results from Euler beam elements, which as expected, are also very close to the analytical Timoshenko beam partition with the hard-interface approximation.

The results for the $k_\sigma = 10^2$ GPa/mm linear elastic interface are presented in Tables 5 and 6. The effect of reducing the interface spring stiffness can now be observed. The Timoshenko beam element simulations with the very large shear modulus $G_{xz} = 10^4\,\text{GPa}$ converge towards the analytical Euler beam partition results very slowly. The convergence is much slower now that the interface stiffness is an order of magnitude smaller. For rigid interfaces, only 11 elements along the DCB were able to give excellent agreement with the analytical results. However, here the very fine non-uniform mesh with 1310 elements is not able to achieve the same degree of agreement. There is of course no comparison in CPU computing time between the two meshes. When Timoshenko beam elements with the normal shear modulus of $G_{xz} = 1/2.6\,\text{GPa}$ are used, the results are close to analytical Timoshenko beam partition, which as expected are once again close to the Euler beam numerical results.

3.3. Linear elastic interfaces with tip shear forces

In the present theories, shear forces cause additional contributions to both the mode I and mode II ERRs, which have been considered in detail in Section 2. In this section, the same two linear elastic interfaces as before are considered, corresponding to the interface stiffness values $k_\sigma = 10^3$ GPa/mm and $k_\sigma = 10^2$ GPa/mm.

The results for the DCB with the $k_\sigma = 10^3$ GPa/mm linear elastic interface and tip shear forces $P_1 = 1\,\text{kN}$ and P_2, which was varied from −10 to 10, are presented in Tables 7 and 8. As shown by Eq. (19), the analytical Euler G_{II} partition depends on the interface constitutive law when shear forces are present. It can be calculated in a completely analytical way by means of Eq. (19). As shown by Eq. (33), the analytical Euler G_I partition depends on $\overline{w}_B^{(1)}$, which depends on the interface constitutive law. This parameter could be determined from FEM simulations and used as an argument to Eq. (33), however in the case of non-rigid hard interfaces, the second term in Eq. (33) is very small and is found to be negligible. The analytical Euler G_I partition is therefore approximately given by just the first term in Eq. (33), which is completely analytical.

The analytical Timoshenko beam G_{II} partitions are the same as the analytical Euler beam G_{II} partitions. The G_I partition, which is given by Eq. (49) and which depends on $\overline{w}_B$ and $\overline{w}_B^{(1)}$, is calculated in the same way as in the previous section for DCBs with tip bending moments by assuming a non-rigid hard interface.

The Timoshenko beam element simulations with the very large shear modulus $G_{xz} = 10^4$ GPa converge slowly towards the analytical Euler beam partition theory. The Timoshenko beam elements with a normal shear modulus $G_{xz} = 1/2.6$ GPa converge slowly towards the analytical Timoshenko beam partition theory. In both cases, a large number of elements in the vicinity of the crack tip are required to obtain this good agreement. In this case where $k_\sigma = 10^3$ GPa/mm, the difference between the Euler and Timoshenko partitions is small.

The results for the $k_\sigma = 10^2$ GPa/mm linear elastic interface are presented in Tables 9 and 10. The Timoshenko beam element simulations with the very large shear modulus $G_{xz} = 10^4$ GPa converge towards the analytical Euler beam partition results very slowly. The Timoshenko beam elements with a normal shear modulus $G_{xz} = 1/2.6$ GPa converge very slowly towards the analytical Timoshenko beam partition theory.

4. Numerical tests with the 2D elasticity partition theory

To validate the analytical 2D elasticity partition theory, FEM simulations were carried out using SIMULIA's Abaqus with reduced-integration QUAD4 elements. The ERR and its partitions were calculated by means of the crack closure technique. The tests were carried out on the DCB shown in Fig. 1a. The Young's modulus is $E = 1$ GPa, the Poisson's ratio is $\nu = 0.3$ and the shear modulus $G_{xz} = E/[2(1+\nu)] = 1/2.6$ GPa. The intact length is $L = 100$ mm, the crack length is $a = 10$ mm and the width is $b = 1$ mm. The total thickness $h = h_1 + h_2$, the thickness ratio $\gamma = h_2/h_1$ and the stiffness ratios $k_{er\sigma} = k_\sigma / E$ and $k_{er\tau} = k_\tau / E$ are all specified separately for each of the following tests. All the finite element meshes had 1100 uniformly distributed QUAD4 elements along the length. The meshes through the thicknesses of both top and bottom beams were also uniform and are specified separately for each of the following tests. The interface was modelled with the four-node quadrilateral cohesive elements (COH2D4) in Abaqus, which were 10^{-5} m thick. The interface had the same distribution of COH2D4 elements along the length as the QUAD4 elements and one element through the thickness.

4.1. The definition of a hard interface

The aim of this test was to give a clearer definition of what constitutes a hard interface in terms of the $k_{er} = k_\sigma / E = k_\tau / E$ ratio. The DCB is the one described at the beginning of Section 4. The total thickness $h = h_1 + h_2$ is 2 mm and the thickness ratio $\gamma = h_2/h_1$ is fixed at 3. The number of finite elements used through the thickness of the top and bottom beams was 15 each. A linear elastic interface constitutive law was also used. The θ_{1NR} pure mode I and the β_{1NR} pure mode II were considered, which represent two extreme cases. The nine stiffness ratios of $k_{er} = k_\sigma / E = k_\tau / E = 10^{-4}$ m^{-1}, 10^{-3} m^{-1}, 10^{-2} m^{-1}, 10^{-1} m^{-1}, 10^{0} m^{-1}, 10^{1} m^{-1}, 10^{2} m^{-1}, 10^{3} m^{-1} and 10^{4} m^{-1} were considered. The ratios $k_{er} = 10^3$ m^{-1} and $k_{er} = 10^4$ m^{-1} represented a nearly rigid or rigid interface, and the ratios $k_{er} = 10^{-4}$ m^{-1} and $k_{er} = 10^{-3}$ m^{-1} represented a very soft interface. The total fracture ERR was set to be 200 kN/mm in the simulations. The test results are recorded in Table 11. The labels 'Li' and 'An' denote the numerical results from the linear interface constitutive law and the results from the analytical partition theory for 2D elasticity respectively. The pure mode I θ_{1NR} is observed to be very pure throughout the entire range of k_{er} values tested. However, the ERR values for very soft interfaces, i.e. $k_{er} = 10^{-4}$ m^{-1} and

$k_{er} = 10^{-3}$ m^{-1}, and nearly rigid or rigid interfaces, i.e. $k_{er} = 10^{3}$ m^{-1} and $k_{er} = 10^{4}$ m^{-1}, are considerably lower than the analytical values. Also, the pure mode II β_{1NR} is observed to be very pure throughout the entire range of k_{er} values tested. However, the ERR values for very soft interfaces, i.e. $k_{er} = 10^{-4}$ m^{-1} and $k_{er} = 10^{-3}$ m^{-1}, and soft interfaces, i.e. $k_{er} = 10^{-2}$ m^{-1}, and nearly rigid or rigid interfaces, i.e. $k_{er} = 10^{3}$ m^{-1} and $k_{er} = 10^{4}$ m^{-1}, and very hard interfaces, i.e. $k_{er} = 10^{2}$ m^{-1}, are considerably lower than the analytical values. It has been shown in Ref. [31] that the ERR values for rigid interfaces are accurately predicted by 2D FEM when using point interface springs. Consequently, the disagreement here is certainly due to numerical errors involved in COH2D4 elements in Abaqus for large k_{er} values. The cause of the disagreement for soft interfaces is not clear. One possible reason is the inaccuracy of the analytical calculation for ERR in Eq. (1) for soft interfaces. This test suggests that a hard interface may be represented by the range 10^{-2} m^{-1} $< k_{er} < 10^{2}$ m^{-1}. Also, note that although the total fracture ERR was set to be 200 kN/mm, slightly smaller loads were applied in the tests to avoid overshooting of 200 kN/mm which causes numerical breakdown in Abaqus. This explains why all the total ERRs, including the analytical ones, are slightly less than 200 kN/mm.

4.2. The effect of the assumption that $k_{er} = k_\sigma / E = k_\tau / E$

In the current 2D elasticity partition theory, it is assumed that $k_{er} = k_\sigma / E = k_\tau / E$. The effect of this assumption was investigated in this numerical test. The same DCB properties and the same FEM meshes as those in Section 4.1 were used. A linear elastic interface constitutive law was also used. Again, pure mode I θ_{1NR} and pure mode II β_{1NR} were considered, which represent two extreme cases. The study on the effect on θ_{1NR} is presented in Table 12. DCB tip bending moments M_1 and M_2 were applied in the ratio θ_{1NR} so that $M_2 = \theta_{1NR} M_1$. The pure mode I θ_{1NR} value was calculated from Eq. (61) with $k_{er} = k_{er\sigma} = k_\sigma / E$ for three values of $k_{er\sigma}$, namely $k_{er\sigma} = 0.1$ m^{-1}, 1 m^{-1}, and 10 m^{-1}. Five k_τ / k_σ ratios were considered, namely $k_\tau / k_\sigma = 10^{-2}$, 10^{-1}, 10^{0}, 10^{1} and 10^{2}. It is seen that the effect of $k_\sigma \neq k_\tau$ is generally small, except for the case when $k_\tau / k_\sigma = 10^{2}$. A recent experiment study [12] showed that typically $k_{er\sigma} = k_\sigma / E \approx 4.5$ m^{-1} and $k_\tau / k_\sigma \approx 0.4 << 10^{2}$. Similarly, the study on the effect on β_{1NR} is also presented in Table 12. DCB tip bending moments M_1 and M_2 were applied in the ratio β_{1NR} so that $M_2 = \beta_{1NR} M_1$. The pure mode II β_{1NR} value was calculated from Eq. (63) with $k_{er} = k_{er\tau} = k_\tau / E$ for three values of $k_{er\tau}$, namely $k_{er\tau} = 0.1$ m^{-1}, 1 m^{-1}, and 10 m^{-1}. Five k_σ / k_τ ratios were considered, namely $k_\sigma / k_\tau = 10^{-2}$, 10^{-1}, 10^{0}, 10^{1} and 10^{2}. It is again seen that the effect of $k_\sigma \neq k_\tau$ is generally small, except for the case of $k_\sigma / k_\tau = 10^{-2}$. A recent experiment study [12] showed that typically $k_{er\tau} = k_\tau / E \approx 1.8$ m^{-1} and $k_\sigma / k_\tau \approx 2.5 >> 10^{-2}$. Within this typical experimental range, the assumption that $k_{er} = k_\sigma / E = k_\tau / E$ gives excellent pureness.

4.3. The pureness of the four pure modes, θ_{1NR}, θ_{2NR}, β_{1NR} and β_{2NR}, given in Eqs. (61) to (64)

This group of numerical tests aimed to validate that the four pure modes, that is the θ_{1NR}, θ_{2NR}, β_{1NR} and β_{2NR} modes given in Eqs. (61) to (64), are independent of the type of interface

constitutive law. The DCB is the one described at the beginning of Section 4. The total thickness is $h = h_1 + h_2 = 5\,\text{mm}$. Two thickness ratios, $\gamma = h_2/h_1 = 2$ and 6, and five stiffness ratios, $k_{er} = k_\sigma / E = k_\tau / E = 0.1$, 0.5, 1, 5 and 10 were considered. The linear, bi-linear and exponential interface constitutive laws in Abaqus were used [35]. The total fracture ERR was again set to be 200 kN/mm, which in the cases of the bi-linear and exponential interface constitutive laws, was equally divided between the linear elastic part and the softening part. The number of finite elements through the thickness of the top beam was fixed to 30 with a uniform mesh distribution. The number of evenly distributed elements through the thickness of the bottom beam was 17 and 22 for $\gamma = 2$ and 6 respectively. That is, the finite element size was always smaller than 0.2 mm. Table 13 shows the excellent pureness of the pure mode pair θ_{1NR} and β_{1NR}, while Table 14 shows the excellent pureness of the pure mode pair θ_{2NR} and β_{2NR}. The labels 'Li', 'Bi', 'Ex' and 'An' in Tables 13 and 14 denote the numerical results from the linear, bi-linear and exponential interface constitutive laws in Abaqus [35] and the results from the analytical partition theory for 2D elasticity, respectively. Similar to the observations in Section 4.1 from Table 11, for very soft interfaces, i.e. $k_{er} = 10^{-4}\ \text{m}^{-1}$ and $k_{er} = 10^{-3}\ \text{m}^{-1}$, and for nearly rigid or rigid interfaces, i.e. $k_{er} = 10^{3}\ \text{m}^{-1}$ and $k_{er} = 10^{4}\ \text{m}^{-1}$, these modes still have excellent pureness but the ERR is significantly lower than the analytical results.

4.4. Partition of mixed modes

This group of numerical tests aimed to validate the analytical mixed-mode partition theory for 2D elasticity. Five different numerical tests were carried out on the DCB described at the beginning of Section 4. The total thickness is $h = h_1 + h_2 = 2\,\text{mm}$ and the thickness ratio $\gamma = h_2/h_1$ was varied according to which test was being carried out. Because the pureness of the pure modes, i.e. the θ_{1NR}, θ_{2NR}, β_{1NR} and β_{2NR} modes, is independent of the form of interface constitutive laws as shown in Section 4.3, only a linear interface constitutive law was considered in the first four tests. The stiffness of the cohesive interface was $k_\sigma = 0.1\,\text{GPa/m}$, which corresponds to an interface stiffness ratio of $k_{er} = 0.1\,\text{m}^{-1}$. The fifth test used a bilinear interface constitutive law. Details are given later.

In the first test in this section, the thickness ratio was set to $\gamma = 2$ and the DCB was subjected to three different loading configurations. There were 7 elements through the thickness of the top beam and 13 elements through the thickness of the bottom beam.

In the first loading configuration of the first test, only bending moments were applied to the DCB tip with $M_1 = 1\,\text{Nm}$ and M_2 varied between -10 Nm and 10 Nm. The values of G_I and G_I/G from 2D FEM simulations and from the analytical mixed-mode partition theory for 2D elasticity are given in Table 15. The 2D FEM simulations and the analytical mixed-mode partition theory for 2D elasticity are in excellent agreement for all values of M_2.

In the second loading configuration of the first test, $M_1 = 1\,\text{Nm}$ and N_1 was varied between -0.5 kN and 0.5 kN. The results are given in Table 16. Again, the values of G_I and G_I/G from the analytical 2D elasticity partition theory are in excellent agreement with the 2D FEM results.

In the third loading configuration of the first test, only shear forces were applied at the DCB tip with $P_1 = 1\,\text{N}$ and P_2 varied between -10 N and 10 N. This resulted in both bending moments and shear forces at the crack tip. Therefore in this loading configuration, G_{I2D}^P and G_{II2D}^P also exist due to the crack tip shear forces. The results from the 2D FEM simulations and the

analytical 2D elasticity partition theory are given in Table 17. Again, excellent agreement is observed.

In the second test in this section, bending moments were applied at the DCB tip, $M_1 = 1\,\text{Nm}$ and $M_2 = 0$, and γ was varied from 1 to 9. There were always ten uniformly distributed QUAD4 elements through the thickness of the top beam. Through the thickness of the bottom beam, there were 10, 13, 15, 16, 17, 17, 18, 18 and 18 uniformly distributed QUAD4 elements for $\gamma = 1$, 2, 3, 4, 5, 6, 7, 8, and 9 respectively. The results from the 2D FEM simulations and the analytical 2D elasticity partition theory are given in Table 18. The agreement is excellent.

In the third test, shear forces were applied at the DCB tip, $P_1 = 1\,\text{N}$ and $P_2 = 0$, and γ was varied from 1 to 9. The same meshes were used as for the second test. The results from the 2D FEM simulations and the analytical 2D elasticity partition theory are given in Table 19. The agreement is excellent.

In the fourth test, the loading condition is the same as that in the second test, i.e. $M_1 = 1\,\text{Nm}$ and $M_2 = 0$. The thickness ratio γ was varied from 7 to 1/7 and the stiffness ratio k_{er} was varied from 0.1 to 10. The same meshes were used as for the second test. The results from the 2D FEM simulations and the analytical 2D elasticity partition theory are given in Table 20. Again, the agreement is excellent for $\gamma \geq 1$ and is good for $\gamma < 1$.

The fifth and final test investigated the accuracy of the analytical mixed-mode partition theory for 2D elasticity when the interface is described by the bilinear interface constitutive law in Abaqus [35]. The DCB and the mesh are the same as the $\gamma = 3$ case from the second test in this section. For the bilinear interface constitutive law, $k_\sigma = k_\tau$ was assumed. The quadratic stress criterion in Abaqus [35] was used to determine the onset of damage, as given by:

$$\left(\frac{\sigma_n}{\sigma_n^0}\right)^2 + \left(\frac{\tau_\sigma}{\tau_s^0}\right)^2 = 1 \tag{82}$$

Two values for the mode-independent total fracture ERR were specified: firstly $G_c = 1000\,\text{kN/mm}$ and secondly $G_c = 4000\,\text{kN/mm}$. In both cases, 200 kN/mm of the total fracture ERR was from the linear elastic part of the interface constitutive law, and the remaining amount was from the softening part. This condition provided the cracking stresses σ_n^0 and τ_s^0 in Eq. (82) as $\sigma_n^0 = \tau_s^0 = \sqrt{400 k_\sigma}$. Three different values for $k_{er} = k_\sigma / E = k_\tau / E$ were used, which were $k_{er} = 0.1\,\text{m}^{-1}$, $1\,\text{m}^{-1}$ and $10\,\text{m}^{-1}$. One bending moment M_1 was applied to the upper beam to produce the total fracture ERR.

Two methods were used to calculate the ERR partition. The first method considers the stresses and relative displacements at the crack tip over the loading history, called here, a 'crack tip analysis'. The second considers the stresses and relative displacement ahead of the crack tip over the damaged region, called here, a 'spatial analysis'. The two methods are expected to give the same partitions of ERR. Note that in all the previous numerical tests, the crack tip analysis was used to calculate the ERR partition. This is consistent with the theoretical developments in Section 2. When a linear interface constitutive law was used in those tests, the two methods gave identical partitions, and therefore only the results from the crack tip analysis were presented in Tables 15 to 20.

Table 21 compares the results from the two methods when there is a bilinear interface constitutive law. Generally, the results from the spatial analysis agree very well with the analytical partitions and are much closer than the crack tip analysis. This is consistent with the findings in Ref. [36]. The analytical partitions work equally well for $G_c = 1000\,\text{kN/mm}$ as for

$G_c = 4000\,\mathrm{kN/mm}$, showing that the size of the damaged region does not have a significant effect for the ranges of G_c and k_{er} examined here.

5. Conclusions

To partition a mixed-mode fracture is of crucial importance for the design of high-integrity structures. In general, fracture toughness is load-dependent. To determine the fracture toughness, the amount of mode I action, and the pure mode I fracture toughness, and the amount of mode II action, and the pure mode II fracture toughness, must all be known. The mode I and mode II fracture toughness can be found from experimental testing, but what loading configurations produce these pure modes? Also, what are the contributions from the mode I and mode II actions in a mixed mode? The focus of this work has been to rigorously derive mixed-mode partition theories for non-rigid cohesive interfaces to answer these questions. Previous work by the authors has focused on rigid interfaces for layered isotropic and laminated composite materials [31-34]. However, the non-rigid cohesive interface represents the majority of interfaces in practical applications. This paper, which addresses non-rigid cohesive interfaces, therefore makes an important contribution to understanding the problem of partitioning mixed-mode fractures.

Within the context of Euler beam theory, when the interface of a layered isotropic DCB is considered to be non-rigid, the two sets of mode I θ and θ' modes coincide on the first set of mode I θ modes. Also, the two sets of mode II β and β' modes coincide on the first set of mode II β modes [31,33]. There is therefore no stealthy interaction between the mode I θ modes and the mode II β modes [31,33]. The total ERR G_E^{NR} consists of two parts G_E^{MN} and G_E^P, i.e. $G_E^{NR} = G_E^{MN} + G_E^P$. G_E^{MN} comes from the crack tip bending moments and axial forces, i.e. M_{1B}, M_{2B}, N_{1B} and N_{2B}, and is readily partitioned into G_{IE}^{MN} and G_{IIE}^{MN} using the mode I θ modes and the mode II β modes [31,33] , i.e. $G_E^{MN} = G_{IE}^{MN} + G_{IIE}^{MN}$ which are independent of interface constitutive laws. Thus, the partition of G_E^{MN} does not depend on interface constitutive laws. G_E^P is due to the crack tip shear forces P_{1B} and P_{2B}, and is partitioned into G_{IE}^P and G_{IIE}^P, i.e. $G_E^P = G_{IE}^P + G_{IIE}^P$. A completely analytical formula for G_{IIE}^P has been derived. It is noted that the partition of G_E^P depends on interface constitutive laws.

Within the context of Timoshenko beam theory, the mode II ERR G_{IIT}^{NR} is the same as that from Euler beam theory, i.e. $G_{IIT}^{NR} = G_{IIE}^{NR}$. The mode I ERR G_{IT}^{NR} however is different due to through-thickness effect. An expression for G_{IT}^{NR} has been derived, which becomes completely analytical for hard interfaces.

Within the context 2D elasticity, one partition theory has been developed. The total ERR G_{2D}^{NR} again consists of two parts G_{2D}^{MN} and G_{2D}^P, i.e. $G_{2D}^{NR} = G_{2D}^{MN} + G_{2D}^P$. G_{2D}^{MN} is partitioned into G_{I2D}^{MN} and G_{II2D}^{MN}, i.e. $G_{2D}^{MN} = G_{I2D}^{MN} + G_{II2D}^{MN}$, using the mode I $\theta_{NR}(k_{er})$ modes and the mode II $\beta_{NR}(k_{er})$ modes which are determined by using the two sets of pure modes from Euler beam theory with rigid interfaces [31,33] and which are independent of the type of interface constitutive law. G_{2D}^P is due to the crack tip shear forces P_{1B} and P_{2B}, and is partitioned into G_{I2D}^P and G_{II2D}^P, i.e. $G^{NR} = G_{I2D}^P + G_{II2D}^P$, which depends on the interface constitutive law.

The theories in this paper provide a valuable method for the study of fracture behavior on non-rigid cohesive interfaces.

Acknowledgement

The authors are very grateful to the reviewers for their comments, which have considerably improved this paper.

References

1. Williams JG. On the calculation of energy release rates for cracked laminates. International Journal of Fracture Mechanics 1988;36:101-19.
2. Schapery RA, Davidson BD. Prediction of energy release rate for mixed-mode delamination using classical plate theory. Applied Mechanics Review 1990;43:S281-7.
3. Suo Z, Hutchinson JW. Interface crack between two elastic layers. International Journal of Fracture Mechanics 1990;43:1-18.
4. Hutchinson JW, Suo Z. Mixed mode cracking in layered materials. Advances in Applied Mechanics 1992;29:63-191.
5. Charalambides M, Kinloch AJ, Wang Y, Williams JG. On the analysis of mixed mode failure. International Journal of Fracture 1992;54:269-91.
6. Thouless MD, Evans AG, Ashby MF, Hutchinson JW. The edge cracking and spalling of brittle plates. Acta Metallurgica 1987;35:1333-41.
7. Thouless MD. Fracture of a model interface under mixed mode loading. Acta Metallurgica et Materialia 1990;35:1135-40.
8. Wang J, Qiao P. Interface crack between two shear deformable elastic layers. Journal of the Mechanics and Physics of Solids 2004;52:891-905.
9. Mollón V, Bonhomme J, Viña J, Argüelles A. Theoretical and experimental analysis of carbon epoxy asymmetric DCB specimens to characterize mixed mode fracture toughness. Polymer Testing 2010;29:766-770.
10. Mollón V, Bonhomme J, Viña J, Argüelles A. Mixed mode fracture toughness: An empirical formulation for G_I/G_{II} determination in asymmetric DCB specimens. Engineering Structures 2010;32:3699-3703.
11. Ouyang Z, Li G. Nonlinear interface shear fracture of end notched flexure specimens. International Journal of solids and Structures 2009;46:2659-68.
12. Ji G, Ouyang Z, Li G. On the interfacial constitutive laws of mixed mode fracture with various adhesive thicknesses. Mechanics of Materials 2012;47:24-32.
13. Ouyang Z, Ji G, Li G. On approximately realizing and characterizing pure mode-I interface fracture between bonded dissimilar materials. Journal of Applied Mechanics 2011;78. Paper No. 031020 (11 pages).
14. Nguyen C, Levy AJ. An exact theory of interfacial debonding in layered elastic composites. International Journal of solids and Structures 2009;46:2712-23.
15. Bennati S, Colleluori M, Corigliano D, Valvo PS, An enhanced beam-theory model of the asymmetric double cantilever beams (ADCB) test for composite laminates. Composite Science and Technology 2009;69:1735-1745.
16. Cornetti P, Mantič V, Carpinteri A. Finite fracture mechanics at elastic interfaces. International Journal of Solids and Structures 2012;49:1022-1032.
17. Weißgraeber P, Becker W. Finite fracture mechanics model for mixed mode fracture in adhesive joints. International Journal of Solids and Structures 2013;50:2383-2394.

18. Zhang Y, Wang S. Buckling, post-buckling and delamination propagation in debonded composite laminates Part 1 Theoretical development. Composite Structures 2009;88:121-30 (Also, a plenary lecture in the 16th International Conference on Composite/Nano Engineering (ICCE-16), July 2008, Kunming, China).
19. Wang S, Zhang Y. Buckling, post-buckling and delamination propagation in debonded composite laminates Part 2 Numerical applications. Composite Structures 2009;88:131-46 (Also, a plenary lecture in the 16th International Conference on Composite/Nano Engineering (ICCE-16), July 2008, Kunming, China).
20. Chen J, Crisfield MA, Kinloch AJ, Busso EP, Matthews FL, Qiu Y. Predicting progressive delamination of composite material specimens via interface elements. Journal of Mechanics of Composite Materials and Structures 1999;6:301-17.
21. Chen J. Predicting progressive delamination of stiffened fibre-composite panel and repaired sandwich panel by decohesion models. Journal of Thermalplastic Composite Materials 2002;15:429-42.
22. Valvo PS. A revised virtual crack closure technique for physically consistent fracture mode partitioning. International Journal of Fracture 2012;173:1-20.
23. Brunner AJ. Experimental aspects mode I and mode II fracture toughness testing of fibre-reinforced polymer-matrix composites. Computer Methods in Applied Mechanics and Engineering 2000; 185:161-72.
24. Blackman ARK, Kingloch AJ, Paraschi M. The determination of mode II adhesive fracture resistance, G_{IIC}, of structural adhesive joints: an effective crack length approach. Engineering Fracrute Mechanics 2005; 72: 877-97.
25. Brunner AJ, Blackman ARK, Williams JG. Calculating a damage parameter and bridging stress from G_{IC} delamination tests on fibre composites. Composites Science and Technology 2006; 66: 785-95.
26. Wang S, Harvey C. Fracture mode partition rules for DCB. 17th Interactional Conference on Composite/Nano Engineering (ICCE-17), July 2009, Honolulu, Hawaii, USA.
27. Harvey C, Wang S. Modelling of delamination propagation in composite laminated beam structures. In: Simos TE, editor. Proceedings of the 7th International Conference of Computational Methods in Science and Engineering (ICCMSE 2009). Rhodes (Greece): American Institute of Physics; 2009.
28. Wang S, Harvey C. Mixed mode partition in one-dimensional fracture. Journal of Key Engineering Materials 2011;462-63:616-21. (Also, a plenary lecture in the 8th International Conference on Fracture and Strength of Solids (FEOFS 2010), 7-9th June 2010, Kuala Lumpur, Malaysia).
29. Wang S, Harvey C. A theory of one-dimensional fracture, Composite Structures 2012;94:758-67. (Also, a plenary lecture in the 16th International Conference on Composite Structures (ICCS16), 28-30th June 2011, Porto, Portugal).
30. Wang S, Guan L. On fracture mode partition theories, Computational Material Sciences 2012;52:240-45.
31. Wang S, Harvey C. Mixed mode partition theories for one dimensional fracture. Engineering Fracture mechanics 2012;79:329-52.
32. Harvey CM, Wang S. Mixed-mode partition theories for one-dimensional delamination in laminated composite beams. Engineering Fracture mechanics 2012;96:737-759.
33. Harvey CM, Wang S. Experimental assessment of mixed-mode partition theories. Composite Structures 2012;94:2057-67.

34. Harvey CM. Mixed-mode partition theories for one-dimensional fracture. PhD Thesis 2012, Department of Aeronautical and Automotive Engineering, Loughborough University, UK.
35. Abaqus Analysis User's Manual Volume IV: Elements. Section 31.5.6: Defining the constitutive response of cohesive elements using a traction-separation description. SIMULIA World Headquarters, 166 Valley Street, Providence, RI 02909-2499, USA:2011.
36. Turon A, Camanho PP, Costa J, Renart J. Accurate simulation of delamination growth under mixed-mode loading using cohesive elements: Definition of interlaminar strengths and elastic stiffness. Composite Structures 2010;92:1857-1864.

Appendix A: The coefficient matrix $[C]$ of the ERR G in Eq. (1)

$$[C]=\frac{1}{Eb^2h_1^3\gamma^3(1+\gamma)^3}\begin{bmatrix} 6\gamma^4\left(\gamma^2+3\gamma+3\right) & -6\gamma^3 & 3h_1\gamma^4 \\ -6\gamma^3 & 6\left(3\gamma^2+3\gamma+1\right) & 3h_1\gamma^4 \\ 3h_1\gamma^4 & 3h_1\gamma^4 & h_1^2\gamma^4\left(\gamma^2-\gamma+1\right)/2 \end{bmatrix} \tag{A1}$$

Appendix B: Higher order interpolations for θ_{1NR} in 2D elasticity theory

By using a cubic spline interpolation in terms of $\log_{10}k_{er}$ with clamped end conditions, passing through $\theta_{1H}(\gamma)$ at $k_{er}=10^3$, passing through $\theta_a(\gamma)$ in Eq. (57) at $k_{er}=10$, passing through $\theta_b(\gamma)$ in Eq. (58) at $k_{er}=1$, passing through $\theta_c(\gamma)$ in Eq. (59) at $k_{er}=0.1$ and passing through $\theta_1'(\gamma)$ in Eq. (7) at $k_{er}=10^{-3}$, the following approximate expressions for $\theta_{1NR}(\gamma,k_{er})$ are obtained:

$$\theta_{1NR}(\gamma,k_{er})=\theta_1' \text{ for } k_{er}\le 10^{-3} \tag{B1}$$

$$\begin{aligned}\theta_{1NR}(\gamma,k_{er})=\theta_1'&-(\log_{10}k_{er}+3)^2\left(\frac{\theta_{1H}}{80}-\frac{9\theta_a}{80}+\frac{\theta_b}{2}-\frac{81\theta_c}{80}+\frac{49\theta_1'}{80}\right)\\&+(\log_{10}k_{er}+3)^3\left(\frac{\theta_{1H}}{160}-\frac{9\theta_a}{160}+\frac{\theta_b}{4}-\frac{61\theta_c}{160}+\frac{29\theta_1'}{160}\right) \text{ for } 10^{-3}\le k_{er}\le 0.1\end{aligned} \tag{B2}$$

$$\begin{aligned}\theta_{1NR}(\gamma,k_{er})=\theta_c&-(\log_{10}k_{er}+1)\left(-\frac{\theta_{1H}}{40}+\frac{9\theta_a}{40}-\theta_b+\frac{21\theta_c}{40}+\frac{11\theta_1'}{40}\right)\\&+(\log_{10}k_{er}+1)^2\left(\frac{\theta_{1H}}{40}-\frac{9\theta_a}{40}+\theta_b-\frac{51\theta_c}{40}+\frac{19\theta_1'}{40}\right)\\&+(\log_{10}k_{er}+1)^3\left(\frac{\theta_{1H}}{20}-\frac{9\theta_a}{20}+\theta_b-\frac{4\theta_c}{5}+\frac{\theta_1'}{5}\right) \text{ for } 0.1\le k_{er}\le 1\end{aligned} \tag{B3}$$

$$\begin{aligned}\theta_{1NR}(\gamma,k_{er})=\theta_b&+(\log_{10}k_{er})\left(-\frac{3\theta_{1H}}{40}+\frac{27\theta_a}{40}-\frac{27\theta_c}{40}+\frac{3\theta_1'}{40}\right)\\&+(\log_{10}k_{er})^2\left(-\frac{\theta_{1H}}{8}+\frac{9\theta_a}{8}-2\theta_b+\frac{9\theta_c}{8}-\frac{\theta_1'}{8}\right)\\&+(\log_{10}k_{er})^3\left(\frac{\theta_{1H}}{5}-\frac{4\theta_a}{5}+\theta_b-\frac{9\theta_c}{20}+\frac{\theta_1'}{20}\right) \text{ for } 1\le k_{er}\le 10\end{aligned} \tag{B4}$$

$$\begin{aligned}\theta_{1NR}(\gamma,k_{er})=\theta_a&+(\log_{10}k_{er}-1)\left(\frac{11\theta_{1H}}{40}+\frac{21\theta_a}{40}-\theta_b+\frac{9\theta_c}{40}-\frac{\theta_1'}{40}\right)\\&+(\log_{10}k_{er}-1)^2\left(\frac{19\theta_{1H}}{40}-\frac{51\theta_a}{40}+\theta_b-\frac{9\theta_c}{40}+\frac{\theta_1'}{40}\right)\\&-(\log_{10}k_{er}-1)^3\left(\frac{29\theta_{1H}}{160}-\frac{61\theta_a}{160}+\frac{\theta_b}{4}-\frac{9\theta_c}{160}+\frac{\theta_1'}{160}\right) \text{ for } 10\le k_{er}\le 10^3\end{aligned} \tag{B5}$$

$$\theta_{1NR}(\gamma,k_{er})=\theta_{1H} \text{ for } k_{er}\ge 10^3 \tag{B6}$$

The pure mode I $\theta_{1H}(\gamma)$ is easily obtained from Suo and Hutchinson [3] as follows:

$$\theta_{1H}(\gamma)=\frac{c_1c_3\left(3\gamma+3\gamma^2+\gamma^3\right)}{c_1c_3+c_2\sqrt{2}\left(3+12\gamma+18\gamma^2+12\gamma^3+3\gamma^4\right)} \tag{B7}$$

where

$$c_1=\sqrt{6\gamma^2+24\gamma^3+36\gamma^4+24\gamma^5+6\gamma^6} \tag{B8}$$

$$c_2=\sin\left(\frac{30\pi-521\pi\gamma}{1800\gamma}\right) \tag{B9}$$

$$c_3=\cos\left(\frac{30\pi-521\pi\gamma}{1800\gamma}\right) \tag{B10}$$

Note that the angles in Eqs. (B9) and (B10) are in radians.

Appendix C: Approximate empirical formulae for the β_P, ξ, θ_P and ζ parameters in Section 2.4

C.1. Interface stiffness ratio $k_{er}=0.1\,\mathrm{m}^{-1}$

The first group of empirical formulae for the β_P, ξ, θ_P and ζ parameters in Section 2.4 are for when $k_{er}=0.1\,\mathrm{m}^{-1}$. The following approximate formulae were obtained by fitting curves to results from FEM simulations in Abaqus. The β_P parameter is given by

$$\beta_P=\beta_1(\gamma)f_1(\gamma)(h+4)^{-f_2(\gamma)/(h+4)} \tag{C1}$$

where $\beta_1(\gamma)$ is given by Eq. (6) and

$$f_1(\gamma)=0.03149\gamma^5-0.5389\gamma^4+3.444\gamma^3-10.14\gamma^2+13.49\gamma-5.288 \tag{C2}$$

$$f_2(\gamma)=0.1149\gamma^5-1.964\gamma^4+12.54\gamma^3-36.90\gamma^2+49.13\gamma-22.93 \tag{C3}$$

The ξ parameter is given by

$$\xi=f_1(\gamma)h^{f_2(\gamma)(h+4)^{f_3(\gamma)/(h+4)}} \tag{C4}$$

where

$$f_1(\gamma)=\left(0.1338\gamma^4-2.382\gamma^3+15.85\gamma^2-47.58\gamma+56.29\right)/(\gamma-0.4913)+0.014 \tag{C5}$$

$$f_2(\gamma)=0.05470\gamma^5-0.9381\gamma^4+5.999\gamma^3-17.63\gamma^2+23.34\gamma-9.329 \tag{C6}$$

$$f_3(\gamma)=-0.1796\gamma^5+3.075\gamma^4-19.64\gamma^3+57.66\gamma^2-76.36\gamma+35.44 \tag{C7}$$

The θ_P parameter is given by

$$\theta_P=\theta_1'f_1(\gamma)(h+4)^{-f_2(\gamma)/(h+4)} \tag{C8}$$

where θ_1' is given by Eq. (7) and

$$f_1(\gamma)=0.0002125\gamma^5-0.004109\gamma^4+0.03068\gamma^3-0.1084\gamma^2+0.2451\gamma+0.8365 \tag{C9}$$

$$f_2(\gamma) = 0.0006145\gamma^5 - 0.01176\gamma^4 + 0.08623\gamma^3 - 0.3025\gamma^2 + 0.6525\gamma - 0.425 \quad \text{(C10)}$$

The ζ parameter is given by

$$\zeta = f_1(\gamma)(h+4)^{f_2(\gamma)/(h+4)} \quad \text{(C11)}$$

where

$$f_1(\gamma) = 0.0009764\gamma^5 - 0.01575\gamma^4 + 0.08514\gamma^3 - 0.1304\gamma^2 - 0.3189\gamma + 1.142 \quad \text{(C12)}$$

$$f_2(\gamma) = -0.01853\gamma^5 + 0.3218\gamma^4 - 2.078\gamma^3 - 6.126\gamma^2 - 8.027\gamma + 3.605 \quad \text{(C13)}$$

C.2. Interface stiffness ratio $k_{er} = 1\,\text{m}^{-1}$

The second group of empirical formulae for the β_P, ξ, θ_P and ζ parameters in Section 2.4 are for when $k_{er} = 1\,\text{m}^{-1}$. The β_P parameter is still given by Eq. (C1) but $f_1(\gamma)$ and $f_2(\gamma)$ in this equation are now given by

$$f_1(\gamma) = 0.006379\gamma^5 - 0.1088\gamma^4 + 0.6918\gamma^3 - 2.026\gamma^2 + 2.669\gamma - 0.2316 \quad \text{(C14)}$$

$$f_2(\gamma) = 0.02669\gamma^5 - 0.4557\gamma^4 + 2.904\gamma^3 - 8.534\gamma^2 + 11.38\gamma - 5.324 \quad \text{(C15)}$$

The ξ parameter is still given by Eq. (C4) but $f_1(\gamma)$, $f_2(\gamma)$ and $f_3(\gamma)$ in this equation are now given by

$$f_1(\gamma) = \left(0.02465\gamma^4 - 0.4575\gamma^3 + 3.224\gamma^2 - 10.42\gamma + 13.5\right)/(\gamma - 0.5787) \quad \text{(C16)}$$

$$f_2(\gamma) = 0.02478\gamma^5 - 0.3947\gamma^4 + 2.372\gamma^3 - 6.623\gamma^2 + 8.479\gamma - 2.318 \quad \text{(C17)}$$

$$f_3(\gamma) = -0.05878\gamma^5 + 0.9543\gamma^4 - 5.835\gamma^3 + 16.55\gamma^2 - 21.53\gamma + 9.921 \quad \text{(C18)}$$

The θ_P parameter still given by Eq. (C8) but $f_1(\gamma)$ and $f_2(\gamma)$ in this equation are now given by

$$f_1(\gamma) = 0.0001309\gamma^5 - 0.003106\gamma^4 + 0.02881\gamma^3 - 0.1176\gamma^2 + 0.4186\gamma + 0.6732 \quad \text{(C19)}$$

$$f_2(\gamma) = 0.000426\gamma^5 - 0.00943\gamma^4 + 0.08126\gamma^3 - 0.3493\gamma^2 + 1.106\gamma - 0.829 \quad \text{(C20)}$$

The ζ parameter is given by Eq. (C11) but $f_1(\gamma)$ and $f_2(\gamma)$ in this equation are now given by

$$f_1(\gamma) = -0.0004163\gamma^5 + 0.009144\gamma^4 - 0.08228\gamma^3 + 0.3929\gamma^2 - 1.063\gamma + 1.485 \quad \text{(C21)}$$

$$f_2(\gamma) = 0.001801\gamma^5 - 0.03328\gamma^4 + 0.2349\gamma^3 - 0.8095\gamma^2 + 1.455\gamma - 0.8212 \quad \text{(C22)}$$

C.3. Interface stiffness ratio $k_{er} = 10\,\text{m}^{-1}$

The third group of empirical formulae for the β_P, ξ, θ_P and ζ parameters in Section 2.4 are for when $k_{er} = 10\,\text{m}^{-1}$. The β_P parameter is still given by Eq. (C1) but $f_1(\gamma)$ and $f_2(\gamma)$ in this equation are now given by

$$f_1(\gamma) = -0.002194\gamma^5 + 0.04798\gamma^4 - 0.3941\gamma^3 + 1.517\gamma^2 - 2.863\gamma + 2.694 \quad \text{(C23)}$$

$$f_2(\gamma) = 0.01229\gamma^5 - 0.131\gamma^4 + 0.2291\gamma^3 + 1.349\gamma^2 - 5.62\gamma + 4.16 \quad \text{(C24)}$$

The ξ parameter is still given by Eq. (C4) but $f_1(\gamma)$, $f_2(\gamma)$ and $f_3(\gamma)$ in this equation are now given by

$$f_1(\gamma) = \left(0.004332^4 - 0.08315\gamma^3 + 0.622\gamma^2 - 2.208\gamma + 3.232\right)/\left(\gamma - 0.6687\right) \quad \text{(C25)}$$

$$f_2(\gamma) = -0.01068029\gamma^5 + 0.213825\gamma^4 - 1.584854\gamma^3 + 5.22858\gamma^2 - 7.21201\gamma + 5.0385 \quad \text{(C26)}$$

$$f_3(\gamma) = 0.01347\gamma^5 - 0.3045\gamma^4 + 2.471\gamma^3 - 8.661\gamma^2 + 12.44\gamma - 5.959 \quad \text{(C27)}$$

The θ_P parameter still given by Eq. (C8) but $f_1(\gamma)$ and $f_2(\gamma)$ in this equation are now given by

$$f_1(\gamma) = 0.0002834\gamma^5 - 0.00633\gamma^4 + 0.05571\gamma^3 - 0.1894\gamma^2 + 0.7786\gamma + 0.3611 \quad \text{(C28)}$$

$$f_2(\gamma) = 0.0009613\gamma^5 - 0.01998\gamma^4 + 0.1636\gamma^3 - 0.6974\gamma^2 + 2.162\gamma - 1.61 \quad \text{(C29)}$$

The ζ parameter is given by Eq. (C11) but $f_1(\gamma)$ and $f_2(\gamma)$ in this equation are now given by

$$f_1(\gamma) = -0.0008008\gamma^5 + 0.01679\gamma^4 - 0.1414\gamma^3 + 0.6151\gamma^2 - 1.475\gamma + 1.816 \quad \text{(C30)}$$

$$f_2(\gamma) = 0.003258\gamma^5 - 0.06094\gamma^4 + 0.4379\gamma^3 - 1.523\gamma^2 + 2.589\gamma - 1.774 \quad \text{(C31)}$$

C.4. Interpolation based on $\log_{10} k_{er}$

In the above, approximations are given for the four parameters β_P, ξ, θ_P and ζ for $k_{er} = 0.1\,\text{m}^{-1}$, $1\,\text{m}^{-1}$ and $10\,\text{m}^{-1}$. By using quadratic interpolation in terms of $\log_{10} k_{er}$ in a similar manner to in Eq. (61), their values can be determined for any intermediate value of k_{er} inside the range $0.1\,\text{m}^{-1} \le k_{er} \le 10\,\text{m}^{-1}$.

Figure Captions

Fig. 1: A DCB with crack influence zone Δa. (a) General description (b) Interface stresses.

Table Captions

Table 1: Comparisons between various analytical partition theories and FEM simulations for the ERR partition G_I/G of a DCB with a rigid interface, $\gamma = 2$, varying M_2 and $M_1 = 1\,\text{Nm}$, $N_1 = 0$, $N_2 = 0$, $P_1 = 0$, $P_2 = 0$.

Table 2: Comparisons between various analytical partition theories and FEM simulations for the mode I ERR G_I of a DCB with a rigid interface, $\gamma = 2$, varying M_2 and $M_1 = 1\,\text{Nm}$, $N_1 = 0$, $N_2 = 0$, $P_1 = 0$, $P_2 = 0$.

Table 3: Comparisons between the analytical beam partition theories and FEM simulations for the ERR partition G_I/G of a DCB with an elastic interface stiffness $k_\sigma = 10^3\,\text{GPa/mm}$, $\gamma = 2$, varying M_2 and $M_1 = 1\,\text{Nm}$, $N_1 = 0$, $N_2 = 0$, $P_1 = 0$, $P_2 = 0$.

Table 4: Comparisons between the analytical beam partition theories and FEM simulations for the mode I ERR G_I of a DCB with an elastic interface stiffness $k_\sigma = 10^3\,\text{GPa/mm}$, $\gamma = 2$, varying M_2 and $M_1 = 1\,\text{Nm}$, $N_1 = 0$, $N_2 = 0$, $P_1 = 0$, $P_2 = 0$.

Table 5: Comparisons between the analytical beam partition theories and FEM simulations for the ERR partition G_I/G of a DCB with an elastic interface stiffness $k_\sigma = 10^2\,\text{GPa/mm}$, $\gamma = 2$, varying M_2 and $M_1 = 1\,\text{Nm}$, $N_1 = 0$, $N_2 = 0$, $P_1 = 0$, $P_2 = 0$.

Table 6: Comparisons between the analytical beam partition theories and FEM simulations for the mode I ERR G_I of a DCB with an elastic interface stiffness $k_\sigma = 10^2\,\text{GPa/mm}$, $\gamma = 2$, varying M_2 and $M_1 = 1\,\text{Nm}$, $N_1 = 0$, $N_2 = 0$, $P_1 = 0$, $P_2 = 0$.

Table 7: Comparisons between the analytical beam partition theories and FEM simulations for the ERR partition G_I/G of a DCB with an elastic interface stiffness $k_\sigma = 10^3\,\text{GPa/mm}$, $\gamma = 2$, varying P_2 and $P_1 = 1\,\text{kN}$, $M_1 = 0$, $M_2 = 0$, $N_1 = 0$, $N_2 = 0$.

Table 8: Comparisons between the analytical beam partition theories and FEM simulations for the mode I ERR G_I of a DCB with an elastic interface stiffness $k_\sigma = 10^3\,\text{GPa/mm}$, $\gamma = 2$, varying P_2 and $P_1 = 1\,\text{kN}$, $M_1 = 0$, $M_2 = 0$, $N_1 = 0$, $N_2 = 0$.

Table 9: Comparisons between the analytical beam partition theories and FEM simulations for the ERR partition G_I/G of a DCB with an elastic interface stiffness $k_\sigma = 10^2\,\text{GPa/mm}$, $\gamma = 2$, varying P_2 and $P_1 = 1\,\text{kN}$, $M_1 = 0$, $M_2 = 0$, $N_1 = 0$, $N_2 = 0$.

Table 10: Comparisons between the analytical beam partition theories and FEM simulations for the mode I ERR G_I of a DCB with an elastic interface stiffness $k_\sigma = 10^2\,\text{GPa/mm}$, $\gamma = 2$, varying P_2 and $P_1 = 1\,\text{kN}$, $M_1 = 0$, $M_2 = 0$, $N_1 = 0$, $N_2 = 0$.

Table 11: The definition of a hard interface with respect to the $k_{er} = k_\sigma / E = k_\tau / E$ ratio.

Table 12: The effect of the assumption that $k_{er} = k_\sigma / E = k_\tau / E$ on the pureness of the θ_{1NR} and β_{1NR} modes.

Table 13: Validation of the pureness of the θ_{1NR} and β_{1NR} modes being independent of the type of interface constitutive law.

Table 14: Validation of the pureness of the θ_{2NR} and β_{2NR} modes being independent of the type of interface constitutive law.

Table 15: Comparisons between the analytical 2D elasticity partition theory and FEM simulations for the ERR partition of a DCB with an elastic interface stiffness $k_{er} = 0.1\,\text{m}^{-1}$, $\gamma = 2$, varying M_2 and $M_1 = 1\,\text{Nm}$, $N_1 = 0$, $N_2 = 0$, $P_1 = 0$, $P_2 = 0$.

Table 16: Comparisons between the analytical 2D elasticity partition theory and FEM simulations for the ERR partition of a DCB with an elastic interface stiffness, $k_{er} = 0.1\,\mathrm{m}^{-1}$, $\gamma = 2$, varying N_1 and $M_1 = 1\,\mathrm{Nm}$, $M_2 = 0$, $N_2 = 0$, $P_1 = 0$, $P_2 = 0$.

Table 17: Comparisons between the analytical 2D elasticity partition theory and FEM simulations for the ERR partition of a DCB with an elastic interface stiffness $k_{er} = 0.1\,\mathrm{m}^{-1}$, $\gamma = 2$, varying P_2 and $P_1 = 1\,\mathrm{N}$, $M_1 = 0$, $M_2 = 0$, $N_1 = 0$, $N_2 = 0$.

Table 18: Comparisons between the analytical 2D elasticity partition theory and FEM simulations for the ERR partition of a DCB with an elastic interface stiffness $k_{er} = 0.1\,\mathrm{m}^{-1}$, varying γ and $M_1 = 1\,\mathrm{Nm}$, $M_2 = 0$, $N_1 = 0$, $N_2 = 0$, $P_1 = 0$, $P_2 = 0$.

Table 19: Comparisons between the analytical 2D elasticity partition theory and FEM simulations for the ERR partition of a DCB with an elastic interface stiffness $k_{er} = 0.1\,\mathrm{m}^{-1}$, varying γ and $P_1 = 1\,\mathrm{N}$, $M_1 = 0$, $M_2 = 0$, $N_1 = 0$, $N_2 = 0$, $P_2 = 0$.

Table 20: Comparison between the analytical 2D elasticity partition theory and FEM simulations for the ERR partition of a DCB with varying k_{er} and γ, and $M_1 = 1\,\mathrm{Nm}$, $M_2 = 0$, $N_1 = 0$, $N_2 = 0$, $P_1 = 0$, $P_2 = 0$.

Table 21: Comparison between the analytical 2D elasticity partition theory and FEM simulations for the ERR partition of a DCB with a single bending moment M_1 with a bilinear constitutive interface law.

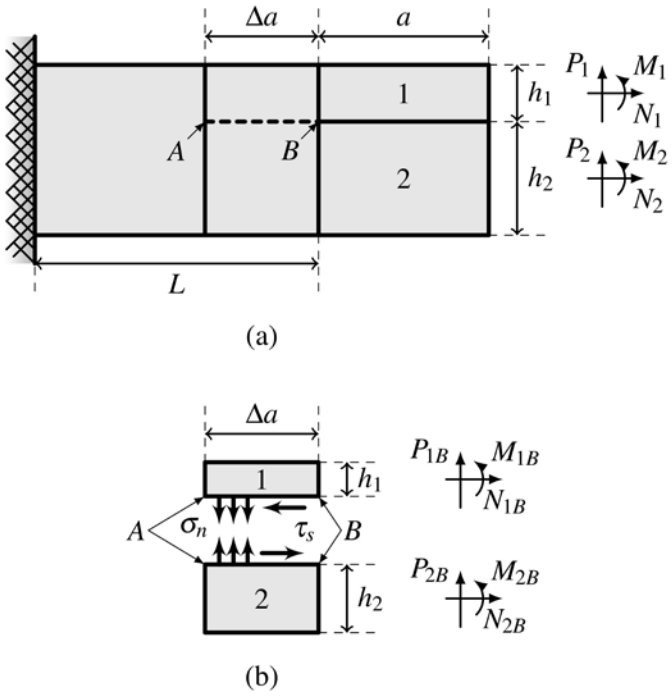

Fig. 1: A DCB with crack influence zone Δa. (a) General description (b) Interface stresses.

Table 1: Comparisons between various analytical partition theories and FEM simulations for the ERR partition G_I/G of a DCB with a rigid interface, $\gamma = 2$, varying M_2 and $M_1 = 1\,\text{Nm}$, $N_1 = 0$, $N_2 = 0$, $P_1 = 0$, $P_2 = 0$.

	$G_I/G\,(\%)$							
M_2 (Nm)	Analytical Euler (rigid interface)	Numerical Euler (11×2 Timo. beams)	Analytical Timo. (rigid interface)	Numerical Timo. (1310×2 Timo. beams)	Numerical Timo. (880×2 Timo. beams)	Averaged Analytical (rigid interface)	2D FEM (440×9 QUAD4s)	2D FEM (220×3 QUAD4s)
−10	71.43	71.43	89.29	89.27	87.78	80.36	80.65	81.39
−8	78.35	78.35	93.04	93.03	91.80	85.70	85.58	86.07
−6	87.85	87.85	97.27	97.26	96.47	92.56	91.87	92.09
−4	100.00	100.00	100.00	100.00	100.00	100.00	98.51	98.60
−2	107.59	107.59	91.46	91.47	92.81	99.53	97.18	97.50
0	76.92	76.92	48.08	48.10	50.51	62.50	60.22	59.03
2	14.29	14.29	3.57	3.58	4.47	8.93	8.98	6.62
4	−7.14	−7.14	3.57	3.56	2.67	−1.79	0.51	1.29
6	−5.53	−5.53	15.20	15.19	13.46	4.84	7.93	10.37
8	0.00	0.00	25.00	24.98	22.90	12.50	15.76	18.76
10	5.13	5.13	32.08	32.06	29.82	18.61	21.85	25.00

Table 2: Comparisons between various analytical partition theories and FEM simulations for the mode I ERR G_I of a DCB with a rigid interface, $\gamma = 2$, varying M_2 and $M_1 = 1\,\text{Nm}$, $N_1 = 0$, $N_2 = 0$, $P_1 = 0$, $P_2 = 0$.

	G_I (kN/mm)							
M_2 (Nm)	Analytical Euler (rigid interface)	Numerical Euler (11×2 Timo. beams)	Analytical Timo. (rigid interface)	Numerical Timo. (1310×2 Timo. beams)	Numerical Timo. (880×2 Timo. beams)	Averaged Analytical (rigid interface)	2D FEM (440×9 QUAD4s)	2D FEM (220×3 QUAD4s)
−10	45.00	45.00	56.25	56.24	55.30	50.63	50.13	47.95
−8	33.78	33.78	40.11	40.11	39.58	36.94	36.37	34.54
−6	24.11	24.11	26.69	26.69	26.48	25.40	24.82	23.32
−4	16.00	16.00	16.00	16.00	16.00	16.00	15.46	14.30
−2	9.44	9.44	8.03	8.03	8.15	8.74	8.31	7.47
0	4.44	4.44	2.78	2.78	2.92	3.61	3.36	2.84
2	1.00	1.00	0.25	0.25	0.31	0.63	0.61	0.39
4	−0.89	−0.89	0.44	0.44	0.33	−0.22	0.06	0.14
6	−1.22	−1.22	3.36	3.36	2.98	1.07	1.72	2.09
8	0.00	0.00	9.00	8.99	8.24	4.50	5.58	6.22
10	2.78	2.78	17.36	17.35	16.13	10.07	11.64	12.55

Table 3: Comparisons between the analytical beam partition theories and FEM simulations for the ERR partition G_I/G of a DCB with an elastic interface stiffness $k_\sigma = 10^3$ GPa/mm, $\gamma = 2$, varying M_2 and $M_1 = 1\,\text{Nm}$, $N_1 = 0$, $N_2 = 0$, $P_1 = 0$, $P_2 = 0$.

	$G_I/G\,(\%)$			
M_2 (Nm)	Analytical Euler (non-rigid elastic interface)	Numerical Euler (1310×2 Timo. beams)	Analytical Timo. (non-rigid elastic interface)	Numerical Timo. (1310×2 Timo. beams)
−10	89.29	89.38	88.78	89.04
−8	93.04	93.03	92.71	92.82
−6	97.27	97.17	97.14	97.12
−4	100.00	99.99	100.00	100.00
−2	91.46	92.37	91.17	91.80
0	48.08	50.46	47.65	48.77
2	3.57	4.11	3.87	3.78
4	3.57	3.50	3.00	3.42
6	15.20	15.45	13.90	14.95
8	25.00	25.50	23.39	24.71
10	32.08	32.72	30.35	31.78

Table 4: Comparisons between the analytical beam partition theories and FEM simulations for the mode I ERR G_I of a DCB with an elastic interface stiffness $k_\sigma = 10^3$ GPa/mm, $\gamma = 2$, varying M_2 and $M_1 = 1\,\text{Nm}$, $N_1 = 0$, $N_2 = 0$, $P_1 = 0$, $P_2 = 0$.

	G_I (kN/mm)			
M_2 (Nm)	Analytical Euler (non-rigid elastic interface)	Numerical Euler (1310×2 Timo. beams)	Analytical Timo. (non-rigid elastic interface)	Numerical Timo. (1310×2 Timo. beams)
−10	56.25	55.14	53.38	52.27
−8	40.11	39.37	38.14	37.30
−6	26.69	26.24	25.45	24.85
−4	16.00	15.77	15.32	14.92
−2	8.03	7.95	7.75	7.51
0	2.78	2.78	2.73	2.62
2	0.25	0.27	0.27	0.25
4	0.44	0.40	0.37	0.39
6	3.36	3.19	3.03	3.06
8	9.00	8.63	8.24	8.25
10	17.36	16.73	16.01	15.96

Table 5: Comparisons between the analytical beam partition theories and FEM simulations for the ERR partition G_I/G of a DCB with an elastic interface stiffness $k_\sigma = 10^2$ GPa/mm, $\gamma = 2$, varying M_2 and $M_1 = 1\,\text{Nm}$, $N_1 = 0$, $N_2 = 0$, $P_1 = 0$, $P_2 = 0$.

	$G_I/G\,(\%)$			
M_2 (Nm)	Analytical Euler (non-rigid elastic interface)	Numerical Euler (1310×2 Timo. beams)	Analytical Timo. (non-rigid elastic interface)	Numerical Timo. (1310×2 Timo. beams)
−10	89.29	87.60	87.55	88.32
−8	93.04	91.68	91.90	92.24
−6	97.27	96.41	96.82	96.74
−4	100.00	99.95	100.00	99.98
−2	91.46	92.48	90.51	92.31
0	48.08	49.66	46.70	49.63
2	3.57	4.34	4.56	4.16
4	3.57	2.72	1.93	3.03
6	15.20	13.34	11.21	14.13
8	25.00	22.64	19.93	23.71
10	32.08	29.49	26.56	30.68

Table 6: Comparisons between the analytical beam partition theories and FEM simulations for the mode I ERR G_I of a DCB with an elastic interface stiffness $k_\sigma = 10^2$ GPa/mm, $\gamma = 2$, varying M_2 and $M_1 = 1\,\text{Nm}$, $N_1 = 0$, $N_2 = 0$, $P_1 = 0$, $P_2 = 0$.

	G_I (kN/mm)			
M_2 (Nm)	Analytical Euler (non-rigid elastic interface)	Numerical Euler (1310×2 Timo. beams)	Analytical Timo. (non-rigid elastic interface)	Numerical Timo. (1310×2 Timo. beams)
−10	56.25	52.65	47.45	54.35
−8	40.11	37.67	34.04	38.84
−6	26.69	25.19	22.86	25.93
−4	16.00	15.21	13.90	15.62
−2	8.03	7.74	7.15	7.91
0	2.78	2.77	2.63	2.80
2	0.25	0.30	0.32	0.28
4	0.44	0.33	0.24	0.37
6	3.36	2.87	2.37	3.05
8	9.00	7.91	6.72	8.33
10	17.36	15.45	13.29	16.21

Table 7: Comparisons between the analytical beam partition theories and FEM simulations for the ERR partition G_I/G of a DCB with an elastic interface stiffness $k_\sigma = 10^3$ GPa/mm, $\gamma = 2$, varying P_2 and $P_1 = 1\,\text{kN}$, $M_1 = 0$, $M_2 = 0$, $N_1 = 0$, $N_2 = 0$.

	$G_I/G\,(\%)$			
$P_2\,(\text{kN})$	Analytical Euler (non-rigid elastic interface)	Numerical Euler (1310×2 Timo. beams)	Analytical Timo. (non-rigid elastic interface)	Numerical Timo. (1310×2 Timo. beams)
−10	89.31	89.61	90.30	90.24
−8	93.06	93.19	93.73	93.64
−6	97.27	97.23	97.55	97.45
−4	100.00	99.99	100.00	100.00
−2	91.44	92.56	92.23	92.75
0	48.01	51.09	50.57	52.06
2	3.56	4.20	3.86	4.28
4	3.56	3.59	4.04	3.89
6	15.17	15.80	16.74	16.72
8	24.95	26.00	27.16	27.26
10	32.03	33.30	34.55	34.71

Table 8: Comparisons between the analytical beam partition theories and FEM simulations for the mode I ERR G_I of a DCB with an elastic interface stiffness $k_\sigma = 10^3$ GPa/mm, $\gamma = 2$, varying P_2 and $P_1 = 1\,\text{kN}$, $M_1 = 0$, $M_2 = 0$, $N_1 = 0$, $N_2 = 0$.

	G_I (kN/mm)			
$P_2\,(\text{kN})$	Analytical Euler (non-rigid elastic interface)	Numerical Euler (1310×2 Timo. beams)	Analytical Timo. (non-rigid elastic interface)	Numerical Timo. (1310×2 Timo. beams)
−10	5625.00	5673.35	6270.07	5979.94
−8	4011.11	4049.91	4469.68	4267.03
−6	2669.44	2699.56	2973.25	2842.52
−4	1600.00	1622.10	1780.79	1706.33
−2	802.78	817.57	892.29	858.51
0	277.78	285.99	307.76	299.04
2	25.00	27.35	27.20	27.93
4	44.44	41.64	50.60	45.19
6	336.11	328.87	377.96	350.84
8	900.00	889.01	1009.29	944.77
10	1736.11	1722.17	1944.59	1827.11

Table 9: Comparisons between the analytical beam partition theories and FEM simulations for the ERR partition G_I/G of a DCB with an elastic interface stiffness $k_\sigma = 10^2$ GPa/mm, $\gamma = 2$, varying P_2 and $P_1 = 1\,\text{kN}$, $M_1 = 0$, $M_2 = 0$, $N_1 = 0$, $N_2 = 0$.

	$G_I/G\,(\%)$			
$P_2\,(\text{kN})$	Analytical Euler (non-rigid elastic interface)	Numerical Euler (1310×2 Timo. beams)	Analytical Timo. (non-rigid elastic interface)	Numerical Timo. (1310×2 Timo. beams)
−10	89.36	88.03	89.36	89.56
−8	93.09	91.97	93.12	93.08
−6	97.29	96.53	97.31	97.10
−4	100.00	99.95	100.00	99.98
−2	91.39	92.79	91.64	93.24
0	47.87	50.69	49.54	52.93
2	3.54	4.47	4.53	4.68
4	3.54	2.88	2.77	3.48
6	15.10	13.90	13.84	15.87
8	24.85	23.46	23.58	26.22
10	31.91	30.44	30.72	33.59

Table 10: Comparisons between the analytical beam partition theories and FEM simulations for the mode I ERR G_I of a DCB with an elastic interface stiffness $k_\sigma = 10^2$ GPa/mm, $\gamma = 2$, varying P_2 and $P_1 = 1\,\text{kN}$, $M_1 = 0$, $M_2 = 0$, $N_1 = 0$, $N_2 = 0$.

	G_I (kN/mm)			
$P_2\,(\text{kN})$	Analytical Euler (non-rigid elastic interface)	Numerical Euler (1310×2 Timo. beams)	Analytical Timo. (non-rigid elastic interface)	Numerical Timo. (1310×2 Timo. beams)
−10	5625.00	5546.02	5624.94	6255.91
−8	4011.11	3967.02	4025.44	4470.30
−6	2669.44	2651.98	2692.89	2983.98
−4	1600.00	1600.83	1627.30	1797.05
−2	802.78	813.58	828.66	909.46
0	277.78	290.24	296.98	321.23
2	25.00	30.79	32.26	32.36
4	44.44	35.26	34.50	42.84
6	336.11	303.63	303.69	352.67
8	900.00	835.88	839.84	961.89
10	1736.11	1632.07	1642.94	1870.44

Table 11: The definition of a hard interface with respect to the $k_{er} = k_\sigma / E = k_\tau / E$ ratio.

	$M_2/M_1 = \theta_{1NR}$		Abaqus (Linear interface law)		Analytical	
$k_{er}\,(1/\mathrm{m})$	$M_1\,(\mathrm{Nm})$	$M_2\,(\mathrm{Nm})$	$G_I\,(\mathrm{kN/mm})$	$G_I/G\,(\%)$	$G_I\,(\mathrm{kN/mm})$	$G_I/G\,(\%)$
10^{-4}	2.00	−2.00	184.9	99.9	199.1	100
10^{-3}	2.00	−2.00	184.9	99.7	199.1	100
10^{-2}	1.98	−2.23	197.6	99.9	197.4	100
10^{-1}	1.96	−2.84	198.3	100.0	198.1	100
10^{0}	1.89	−4.20	199.0	100.0	198.9	100
10^{1}	1.81	−5.43	199.3	100.0	198.8	100
10^{2}	1.66	−7.01	194.0	100.0	198.1	100
10^{3}	1.46	−8.80	164.5	100.0	199.7	100
10^{4}	1.46	−8.80	164.5	100.0	199.7	100

	$M_2/M_1 = \beta_{1NR}$		Abaqus (Linear interface law)		Analytical	
$k_{er}\,(1/\mathrm{m})$	$M_1\,(\mathrm{Nm})$	$M_2\,(\mathrm{Nm})$	$G_I\,(\mathrm{kN/mm})$	$G_I/G\,(\%)$	$G_I\,(\mathrm{kN/mm})$	$G_I/G\,(\%)$
10^{-4}	0.51	13.77	1.227	99.9	196.6	100
10^{-3}	0.51	13.77	11.83	99.9	196.6	100
10^{-2}	0.548	13.81	86.43	99.6	198.8	100
10^{-1}	0.630	13.61	193.2	99.9	196.2	100
10^{0}	0.825	13.29	196.4	99.9	197.4	100
10^{1}	0.995	12.85	196.6	99.9	197.3	100
10^{2}	1.22	12.09	178.8	99.9	198.4	100
10^{3}	1.46	10.88	127.7	99.9	198.5	100
10^{4}	1.46	10.88	108.6	99.9	198.5	100

Table 12: The effect of the assumption that $k_{er} = k_\sigma / E = k_\tau / E$ on the pureness of the θ_{1NR} and β_{1NR} modes.

		$M_2/M_1 = \theta_{1NR}$					$M_2/M_1 = \beta_{1NR}$		
	$k_{er\sigma}$ (1/m)	0.1	1	10		$k_{er\tau}$ (1/m)	0.1	1	10
k_τ/k_σ	M_1 (Nm)	1.96	1.89	1.81	k_σ/k_τ	M_1 (Nm)	0.63	0.825	0.995
	M_2 (Nm)	−2.84	−4.20	−5.43		M_2 (Nm)	13.61	13.29	12.85
10^{-2}	G_I (kN/mm)	197.7	194.5	189.9	10^{-2}	G_I (kN/mm)	183.3	188.3	179.0
	G_I/G (%)	100	99.2	95.2		G_I/G (%)	96.3	94.9	92.3
10^{-1}	G_I (kN/mm)	197.9	195.5	194.1	10^{-1}	G_I (kN/mm)	188.5	195.6	190.3
	G_I/G (%)	100	99.6	97.5		G_I/G (%)	99.1	99.1	98.1
10^{0}	G_I (kN/mm)	198.3	199.0	199.3	10^{0}	G_I (kN/mm)	193.2	196.4	196.6
	G_I/G (%)	100	100	100		G_I/G (%)	99.9	99.9	99.9
10^{1}	G_I (kN/mm)	191.2	189.8	186.6	10^{1}	G_I (kN/mm)	193.2	197.5	192.3
	G_I/G (%)	96.5	95.3	92.7		G_I/G (%)	100	99.6	99.1
10^{2}	G_I (kN/mm)	160.1	161.0	162.4	10^{2}	G_I (kN/mm)	193.2	196.6	192.0
	G_I/G (%)	81.4	81.1	81.9		G_I/G (%)	99.9	99.1	99.1
An	G_I (kN/mm)	198.1	198.9	199.8	An	G_I (kN/mm)	196.2	197.4	197.3
	G_I/G (%)	100	100	100		G_I/G (%)	100	100	100

Table 13: Validation of the pureness of the θ_{1NR} and β_{1NR} modes being independent of the type of interface constitutive law.

$\gamma = 2$		$M_2/M_1 = \theta_{1NR}$					$M_2/M_1 = \beta_{1NR}$				
	k_{er} (1/m)	0.1	0.5	1	5	10	0.1	0.5	1	5	10
	M_1 (Nm)	11.30	11.05	10.95	10.70	10.60	5.85	6.31	6.45	6.80	7.00
	M_2 (Nm)	−14.58	−16.11	−16.65	−17.84	−18.55	39.28	8.82	38.50	37.94	37.67
Li	G_I (kN/mm)	199.9	199.5	199.5	199.5	198.9	194.5	196.4	195.4	195.1	195.5
	G_I/G (%)	100	100	100	100	100	100	100	100	100	100
Bi	G_I (kN/mm)	199.7	199.3	199.0	198.0	198.5	193.4	195.9	194.2	194.1	194.7
	G_I/G (%)	100	100	100	100	100	99.9	99.9	99.9	99.9	99.9
Ex	G_I (kN/mm)	199.7	199.4	199.0	198.2	198.5	193.7	195.6	194.4	194.2	194.2
	G_I/G (%)	100	100	100	100	100	99.9	99.9	99.9	99.9	99.9
An	G_I (kN/mm)	199.4	199.1	198.7	197.5	198.3	196.5	198.0	197.1	197.1	197.6
	G_I/G (%)	100	100	100	100	100	100	100	100	100	100

$\gamma = 6$		$M_2/M_1 = \theta_{1NR}$					$M_2/M_1 = \beta_{1NR}$				
	k_{er} (1/m)	0.1	0.5	1	5	10	0.1	0.5	1	5	10
	M_1 (Nm)	3.45	3.36	3.33	3.20	3.15	0.503	0.875	1.04	1.36	1.50
	M_2 (Nm)	−6.27	−15.31	−19.26	−27.37	−30.71	83.63	82.43	81.80	79.07	78.37
Li	G_I (kN/mm)	199.1	197.6	199.5	198.4	199.8	195.4	195.2	195.7	194.2	196.2
	G_I/G (%)	100	100	100	100	100	99.6	99.6	99.6	99.6	99.6
Bi	G_I (kN/mm)	198.6	196.5	199.0	198.0	198.9	195.0	194.5	195.4	193.7	195.8
	G_I/G (%)	100	100	100	100	100	99.5	99.5	99.5	99.5	99.5
Ex	G_I (kN/mm)	198.6	196.9	199.1	198.0	199.0	194.9	194.4	195.1	193.6	195.7
	G_I/G (%)	100	100	100	100	100	99.5	99.5	99.5	99.5	99.5
An	G_I (kN/mm)	198.6	196.9	198.7	197.7	198.8	197.5	197.4	198.3	196.5	199.0
	G_I/G (%)	100	100	100	100	100	100	100	100	100	100

Table 14: Validation of the pureness of the θ_{2NR} and β_{2NR} modes being independent of the type of interface constitutive law.

$\gamma = 2$		$N_1/M_1 = \theta_{2NR}$					$N_1/M_1 = \beta_{2NR}$				
	k_{er} (1/m)	0.1	0.5	1	5	10	0.1	0.5	1	5	10
	M_1 (Nm)	13.10	13.00	13.00	12.90	12.90	9.4	14.5	16.4	20.6	22.9
	N_1 (kN)	−19.65	−21.64	−22.42	−24.03	−25.01	530.2	521.5	520.6	512.7	508.4
Li	G_I (kN/mm)	198.9	197.2	197.8	196.7	198.0	195.4	195.0	196.9	196.5	196.3
	G_I/G (%)	100	100	100	100	100	99.9	99.9	99.9	99.9	99.9
Bi	G_I (kN/mm)	198.7	197.1	197.7	196.5	197.8	195.1	195.0	196.4	196.0	196.0
	G_I/G (%)	100	100	100	100	100	99.9	99.9	99.9	99.9	99.9
Ex	G_I (kN/mm)	198.7	197.1	197.7	196.5	197.7	195.2	194.9	196.5	196.2	196.1
	G_I/G (%)	100	100	100	100	100	99.9	99.9	99.9	99.9	99.9
An	G_I (kN/mm)	198.7	197.1	197.8	196.6	197.8	196.5	196.0	197.7	197.4	197.5
	G_I/G (%)	100	100	100	100	100	100	100	100	100	100

$\gamma = 6$		$N_1/M_1 = \theta_{2NR}$					$N_1/M_1 = \beta_{2NR}$				
	k_{er} (1/m)	0.1	0.5	1	5	10	0.1	0.5	1	5	10
	M_1 (Nm)	3.48	3.44	3.40	3.33	3.29	0.116	0.495	0.655	1.00	1.13
	N_1 (kN)	−1.706	−4.179	−5.213	−7.459	−8.355	22.80	22.51	22.23	21.66	21.20
Li	G_I (kN/mm)	199.0	198.1	196.9	198.4	198.9	196.4	196.7	195.1	197.0	195.0
	G_I/G (%)	100	100	100	100	100	99.9	99.9	99.9	99.9	99.9
Bi	G_I (kN/mm)	199.0	198.1	196.8	198.4	198.7	195.7	196.4	194.7	196.4	194.6
	G_I/G (%)	100	100	100	100	100	99.9	99.9	99.9	99.9	99.9
Ex	G_I (kN/mm)	199.0	198.0	196.8	198.4	198.7	195.7	196.5	194.9	196.5	194.5
	G_I/G (%)	100	100	100	100	100	99.9	99.9	99.9	99.9	99.9
An	G_I (kN/mm)	198.7	197.9	196.4	198.0	198.5	198.1	198.7	197.5	198.9	196.5
	G_I/G (%)	100	100	100	100	100	100	100	100	100	100

Table 15: Comparisons between the analytical 2D elasticity partition theory and FEM simulations for the ERR partition of a DCB with an elastic interface stiffness $k_{er} = 0.1\,\mathrm{m}^{-1}$, $\gamma = 2$, varying M_2 and $M_1 = 1\,\mathrm{Nm}$, $N_1 = 0$, $N_2 = 0$, $P_1 = 0$, $P_2 = 0$.

$M_2\,(\mathrm{Nm})$	$G_I\,(\mathrm{kN/mm})$		$G_I/G\,(\%)$	
	Analytical 2D elasticity partition theory	2D FEM (QUAD4 elements)	Analytical 2D elasticity partition theory	2D FEM (QUAD4 elements)
−10	106.4	108.3	50.04	51.31
−8	82.45	83.90	56.67	57.96
−6	61.56	62.64	66.46	67.70
−4	43.72	44.48	80.96	81.94
−2	28.92	29.42	97.62	97.89
0	17.17	17.47	88.04	88.06
2	8.464	8.609	35.83	36.45
4	2.806	2.853	6.68	6.89
6	0.1943	0.1971	0.26	0.27
8	0.6295	0.6419	0.52	0.54
10	4.111	4.187	2.25	2.34

Table 16: Comparisons between the analytical 2D elasticity partition theory and FEM simulations for the ERR partition of a DCB with an elastic interface stiffness, $k_{er} = 0.1\,\mathrm{m}^{-1}$, $\gamma = 2$, varying N_1 and $M_1 = 1\,\mathrm{Nm}$, $M_2 = 0$, $N_2 = 0$, $P_1 = 0$, $P_2 = 0$.

	$G_I\,(\mathrm{kN/mm})$		$G_I/G\,(\%)$	
$N_1\,(\mathrm{kN})$	Analytical 2D elasticity partition theory	2D FEM (QUAD4 elements)	Analytical 2D elasticity partition theory	2D FEM (QUAD4 elements)
−0.5	17.29	17.60	90.80	90.76
−0.4	17.27	17.57	90.27	90.24
−0.3	17.24	17.54	89.73	89.71
−0.2	17.22	17.52	89.18	89.17
−0.1	17.19	17.49	88.61	88.62
0	17.17	17.47	88.04	88.06
0.1	17.14	17.44	87.46	87.49
0.2	17.12	17.41	86.87	86.91
0.3	17.10	17.39	86.28	86.33
0.4	17.07	17.36	85.67	85.74
0.5	17.05	17.34	85.06	85.14

Table 17: Comparisons between the analytical 2D elasticity partition theory and FEM simulations for the ERR partition of a DCB with an elastic interface stiffness $k_{er} = 0.1\,\mathrm{m}^{-1}$, $\gamma = 2$, varying P_2 and $P_1 = 1\,\mathrm{N}$, $M_1 = 0$, $M_2 = 0$, $N_1 = 0$, $N_2 = 0$.

	$G_I\,(\mathrm{N/m})$		$G_I/G\,(\%)$	
$P_2\,(\mathrm{N})$	Analytical 2D elasticity partition theory	2D FEM (QUAD4 elements)	Analytical 2D elasticity partition theory	2D FEM (QUAD4 elements)
−10	3.448×10^{4}	3.473×10^{4}	13.87	14.23
−8	2.585×10^{4}	2.606×10^{4}	16.72	17.14
−6	1.847×10^{4}	1.862×10^{4}	22.11	22.66
−4	1.232×10^{4}	1.244×10^{4}	35.00	35.77
−2	7.418×10^{3}	7.493×10^{3}	76.67	77.45
0	3.751×10^{3}	3.796×10^{3}	54.23	54.76
2	1.322×10^{3}	1.344×10^{3}	4.91	5.06
4	1.316×10^{2}	1.370×10^{2}	0.19	0.20
6	1.800×10^{2}	1.755×10^{2}	0.13	0.13
8	1.467×10^{3}	1.459×10^{3}	0.66	0.67
10	3.993×10^{3}	3.988×10^{3}	1.19	1.21

Table 18: Comparisons between the analytical 2D elasticity partition theory and FEM simulations for the ERR partition of a DCB with an elastic interface stiffness $k_{er} = 0.1\,\mathrm{m}^{-1}$, varying γ and $M_1 = 1\,\mathrm{Nm}$, $M_2 = 0$, $N_1 = 0$, $N_2 = 0$, $P_1 = 0$, $P_2 = 0$.

	$G_I\,(\mathrm{kN/mm})$		$G_I/G\,(\%)$	
γ	Analytical 2D elasticity partition theory	2D FEM (QUAD4 elements)	Analytical 2D elasticity partition theory	2D FEM (QUAD4 elements)
1	3.000	3.029	57.14	57.67
2	17.17	17.27	88.04	88.01
3	45.30	45.12	95.87	94.72
4	91.31	90.83	98.18	96.87
5	159.7	159.0	99.05	97.80
6	255.1	254.1	99.44	98.29
7	381.9	380.7	99.65	98.58
8	544.7	543.4	99.76	98.78
9	748.0	746.3	99.83	98.92

Table 19: Comparisons between the analytical 2D elasticity partition theory and FEM simulations for the ERR partition of a DCB with an elastic interface stiffness $k_{er} = 0.1\,\mathrm{m}^{-1}$, varying γ and $P_1 = 1\,\mathrm{N}$, $M_1 = 0$, $M_2 = 0$, $N_1 = 0$, $N_2 = 0$, $P_2 = 0$.

	$G_I\,(\mathrm{N/m})$		$G_I/G\,(\%)$	
γ	Analytical 2D elasticity partition theory	2D FEM (QUAD4 elements)	Analytical 2D elasticity partition theory	2D FEM (QUAD4 elements)
1	8.105×10^{2}	8.137×10^{2}	17.47	17.78
2	3.751×10^{3}	3.759×10^{3}	54.23	54.59
3	8.942×10^{3}	8.912×10^{3}	79.25	78.16
4	1.673×10^{4}	1.666×10^{4}	90.13	88.47
5	2.761×10^{4}	2.751×10^{4}	94.80	93.11
6	4.205×10^{4}	4.192×10^{4}	97.01	95.44
7	6.055×10^{4}	6.040×10^{4}	98.14	96.73
8	8.359×10^{4}	8.343×10^{4}	98.78	97.50
9	1.116×10^{5}	1.114×10^{5}	99.16	98.00

Table 20: Comparison between the analytical 2D elasticity partition theory and FEM simulations for the ERR partition of a DCB with varying k_{er} and γ, and $M_1 = 1\,\mathrm{Nm}$, $M_2 = 0$, $N_1 = 0$, $N_2 = 0$, $P_1 = 0$, $P_2 = 0$.

		Analytical 2D elasticity partition theory					2D FEM (QUAD4 elements)				
γ	$k_{er}\,(1/\mathrm{m})$	0.1	0.5	1	5	10	0.1	0.5	1	5	10
7	$G_I\,(\mathrm{kN/mm})$	381.9	371.5	364.3	355.8	332.0	380.7	375.4	371.8	358.2	349.1
	$G_I/G\,(\%)$	99.65	96.94	95.06	92.83	86.63	98.59	97.46	96.72	94.07	92.39
5	$G_I\,(\mathrm{kN/mm})$	159.7	154.9	152.0	148.6	139.7	159.0	156.4	154.7	148.6	144.7
	$G_I/G\,(\%)$	99.05	96.06	94.24	92.16	86.61	97.80	96.39	95.50	92.44	90.59
3	$G_I\,(\mathrm{kN/mm})$	45.30	43.75	42.99	42.18	40.17	45.12	44.09	43.48	41.47	40.29
	$G_I/G\,(\%)$	95.87	92.59	90.98	89.26	85.01	94.72	92.71	91.56	87.96	85.97
1	$G_I\,(\mathrm{kN/mm})$	3.000	3.000	3.000	3.000	3.000	3.029	3.029	3.028	3.024	3.022
	$G_I/G\,(\%)$	57.14	57.14	57.14	57.14	57.14	57.66	57.60	57.79	58.59	59.22
1/3	$G_I\,(\mathrm{kN/mm})$	97.09	143.9	165.5	187.8	240.9	116.2	146.0	162.7	214.4	242.91
	$G_I/G\,(\%)$	9.45	14.00	16.11	18.27	23.44	11.62	14.40	16.20	22.21	25.93
1/5	$G_I\,(\mathrm{kN/mm})$	17.02	41.69	54.83	69.11	105.3	28.72	40.76	47.92	71.62	85.70
	$G_I/G\,(\%)$	3.12	7.64	10.04	12.66	19.29	5.42	7.62	9.08	14.41	18.04
1/7	$G_I\,(\mathrm{kN/mm})$	5.529	20.70	29.66	39.77	66.31	12.51	19.02	23.10	36.92	45.38
	$G_I/G\,(\%)$	1.50	5.60	8.03	10.76	17.94	3.47	5.28	6.52	11.20	14.56

Table 21: Comparison between the analytical 2D elasticity partition theory and FEM simulations for the ERR partition of a DCB with a single bending moment M_1 with a bilinear constitutive interface law.

		Crack tip analysis			Spatial analysis			Analytical		
G_c (kN/mm)	k_{er} (1/m)	0.1	1	10	0.1	1	10	0.1	1	10
1000	G_I (kN/mm)	966.7	944.9	900.2	950.9	919.3	864.9	958.7	909.8	850.1
	G_{II} (kN/mm)	32.47	54.28	97.26	48.38	79.11	132.4	41.27	90.2	149.9
	G (kN/mm)	999.1	999.2	997.5	999.2	998.4	997.3	1000	1000	1000
	G_I/G (%)	96.75	94.57	90.25	95.16	92.08	86.72	95.87	90.98	85.01
4000	G_I (kN/mm)	3928	3872	3748	3830	3733	3561	3835	3639	3401
	G_{II} (kN/mm)	70.42	125.8	246.7	167.3	261.1	430.4	165.1	360.8	599.5
	G (kN/mm)	3999	3998	3994	3997	3995	3992	4000	4000	4000
	G_I/G (%)	98.24	96.85	93.82	95.82	93.46	89.22	95.87	90.98	85.01